



GEWEX Water Vapor Assessment (G-VAP)

Report on

Assessment of climate time series of total column water vapour against climate indices (VaKaS)

*Ralf Bennartz⁽¹⁾, Frank Fell⁽²⁾, Marc Schroeder⁽³⁾,
Andi Walther⁽⁴⁾, Ulrika Willén⁽⁵⁾*

(1) Vanderbilt University, Nashville, US

(2) Informus GmbH, Berlin, Germany

(3) Deutscher Wetterdienst, Offenbach, Germany

(4) University of Wisconsin, Madison, US

(5) SMHI, Norrköping, Sweden

Document Change Record

Issue/	Date	Change record (author)
--------	------	------------------------

Issue/Revision Index:

1.0

Date:

13/11/2014

Revision		
1.0	13/11/2014	Initial version

Table of Contents

1	Executive summary	4
2	Introduction	4
3	Data	5
3.1	Satellite-based and merged products	5
3.2	Reanalysis products	6
3.3	Climate models	6
3.4	Climate indices	7
4	Methods	9
4.1	Data processing	9
4.2	Statistical significance of correlations	10
5	Results	11
5.1	Statistical assessment of climate indices	11
5.2	Analysis of water vapour datasets	14
5.3	Assessment of ECE and ESM versus other datasets	18
6	Conclusions	23
7	References.....	23
8	Appendix A: Additional figures.....	26
9	Appendix B: Description of output data	34
9.1	[VAKAS root folder]/data	34
9.2	[VAKAS root folder]/results/maps_diff_month_since_1970	34
9.3	[VAKAS root folder]/results/time_series_alldata_regional	36
9.4	[VAKAS root folder]/results/time_series_climate_index	37
9.5	[VAKAS root folder]/results/correlation_maps	37

Purpose

This report summarises the results of the activity “Assessment of climate time series of total column water vapour against climate indices (VaKaS)” which was dedicated to support the GEWEX water vapor assessment (G-VAP). The report is part of the Appendix of the G-VAP final report, and its executive summary may be included in the main part of the final report.

1 Executive summary

A total of eight TCWV datasets were compared against nine climate indices. TCWV datasets included three re-analyses datasets, three purely observational datasets and two climate model datasets. All data sets were collocated on a 1x1 degree grid and comparisons were performed on monthly anomalies for the time period 1988 to 2008. Emphasis was put on identifying regions where TCWV datasets showed significant correlations with the climate indices.

For all climate indices on SST (e.g. ENSO), all data sets agreed well in term of reproducing spatial correlation patterns. For indices based on the atmospheric state (e.g. AO), the climate model data sets showed significantly weaker correlations than the observational or re-analysis datasets.

2 Introduction

In a Joint Letter from the Global Climate Observing System (GCOS) and the World Climate Research Programme (WCRP) the general need for coordinated international assessments of climate products was formulated. Such assessments are important mechanisms for improvements and to enhance and promote utilisation. The GEWEX Data and Assessments Panel (GDAP) has initiated G-VAP in 2011. The major purpose of G-VAP is to:

- Quantify the state of the art in water vapour products being constructed for climate applications, and by this;
- Support the selection process of suitable water vapour products by GDAP for its production of globally consistent water and energy cycle products.

The results of the first two workshops together with feedback from the first GDAP meeting were used for setting up the G-VAP assessment plan. This plan is available at <http://www.gewex-vap.org> and summarizes scope and goals of the assessment, introduces science questions and provides details on the planned technical and scientific activities. The focus of G-VAP is to assess the fitness of long-term satellite based data records for climate applications, mainly through an analysis of their stability and to explain potential inconsistencies among those records.

This report presents the results of the study “Assessment of climate time series of total column water vapour against climate indices (VaKaS)” commissioned by Deutscher Wetterdienst (DWD) in 2013.

In total, eight TCWV climate time series comprising observational data, re-analyses as well as climate model results were analysed against a set of nine climate indices with the aim to evaluate the different TCWV products against the different climate indices and provide information about commonalities and differences between the different datasets.

This report is structured as follows: Section 3 provides a short description of the climate time series and indices used within this study. Section 4 outlines the preparatory processing performed in order to map all datasets onto a common spatial and temporal grid. Section 5 then describes the statistical analysis performed and the results obtained. Appendix A provides correlation maps for all individual datasets and against all climate indices and Appendix B lists all products derived in the context of the present project.

3 Data

A brief description of the eight investigated TCWV climate time series is provided in the following subsections. These datasets can be subdivided into satellite observation based datasets, reanalyses using data assimilation techniques, as well as climate model derived datasets that have been obtained without data assimilation but with prescribed sea surface temperature fields. For detailed information on the individual datasets, we refer to the references provided in the text.

3.1 Satellite-based and merged products

3.1.1 HOAPS

The Hamburg Ocean Atmosphere Parameters and Fluxes from Satellite Data¹ (HOAPS) set [Andersson et al., 2011] is a completely satellite based climatology of precipitation, evaporation and freshwater budget (evaporation minus precipitation) as well as related turbulent heat fluxes and atmospheric state variables over the global ice free oceans. All variables are derived from Special Sensor Microwave Imager (SSM/I) passive microwave radiometers on-board the Defense Meteorological Satellite Program (DMSP) platforms F08, F10, F11, F13, F14 and F15, except for the sea surface temperature (SST), which is taken from Advanced Very High Resolution Radiometer (AVHRR) measurements. HOAPS is only available over the global ice-free oceans.

HOAPS was jointly developed by the University of Hamburg and the Max Planck Institute for Meteorology and has meanwhile successfully been transferred to CM SAF (Satellite Application Facility on Climate Monitoring). The most recent release Version 3.2 is based on homogenized SSM/I observations and covers the years 1987 to 2008.

3.1.2 RSS

The RSS dataset is a merged total column water vapour (TCWV) data set for the global oceans using the version-7 (V7) passive microwave geophysical ocean products [Hilburn and Wentz, 2008] publicly available from Remote Sensing Systems². The product is available from January 1988 to the date of the most recent processing.

The TCWV values come from all SSM/I instruments (F08 through F15), the F16 and F17 Special Sensor Microwave Imager/Sounder (SSMIS), Advanced Microwave Scanning Radiometer for EOS (AMSR-E) and WindSat. These microwave radiometers have been carefully intercalibrated at the brightness temperature level and the V7 ocean products have been produced using a consistent processing methodology for all sensors.

3.1.3 NVAP-M

NASA's Making Earth Science Data Records for Use in Research Environments (MEaSUREs) program³ began in 2008 and has the goal of creating reliable and widely accepted Earth system data records for a variety of geophysical time series. NVAP-M⁴, derived within this framework, refers to the NASA Water Vapor MEaSUREs (briefly NVAP-M) and spans over the time period 1988 to 2009. NVAP-M is further described in Vonder Haar et al. [2012].

Input sources include SSM/I-based TCWV values over ocean, High-resolution Infrared Radiation Sounder (HIRS) water vapour over land and ocean, Atmospheric Infrared Sounder

¹ <http://www.hoaps.zmaw.de/> (URL tested: 2014-09-02)

² http://images.remss.com/ssmi/ssmi_data_daily.html (URL tested: 2014-09-02)

³ <https://earthdata.nasa.gov/our-community/community-data-system-programs/measures-projects> (URL tested: 2014-09-02)

⁴ <http://nvap.stcnet.com/> (URL tested: 2014-09-02)

(AIRS) from 2002 onwards, and observations from the Integrated Global Radiosonde Archive (IGRA).

3.2 Reanalysis products

3.2.1 ERA-Interim

ERA-Interim⁵ (Simmons et al. 2007, Dee et al. 2011) is a third generation global atmospheric reanalysis provided by the European Centre for Medium-Range Weather Forecasts (ECMWF). It improves on previous versions (e.g. ERA-40) by using an improved atmospheric model and assimilation system (ECMWF, 4D-VAR, 2006). The spatial resolution of the data set is approximately 80 km (T255 spectral) on 60 vertical levels from the surface up to 0.1 hPa. Among others, it assimilates a long list of satellite radiances, (e.g. SSM/I and SSMIS). ERA-Interim is available since 1979 and is continuously updated. For this study monthly gridded TCWV products were used.

3.2.2 MERRA

The Modern Era Retrospective-Analysis for Research and Applications (MERRA, Rienecker et al. 2011) was generated with version 5.2.0 of the Goddard Earth Observing System (GEOS) atmospheric model and data assimilation system (DAS). The MERRA time period covers the modern era of remotely sensed data, from 1979 through the present, and the special focus of the atmospheric assimilation is the hydrological cycle. MERRA has a native model resolution of 0.5° (latitude) x 0.667° (longitude) with 72 vertical levels.

3.2.3 CFSR

The Climate System Forecast Reanalysis (CFSR, Saha et al. 2010) is also a third generation global reanalysis product. The CFSR global atmosphere resolution is ~38 km (T382) with 64 vertical levels covering the time period from 1979 to 2010. It includes atmosphere-land-ocean-sea ice coupling and (in addition to assimilating satellite radiances) uses observed precipitation from Climate Prediction Center (CPC) Merged Analysis of Precipitation (CMAP) 5-day mean and daily CPC gauge analysis. The analysis system used in CFSR for the atmosphere, the Grid-point Statistical Interpolation (GSI) scheme, is nearly identical to the one used in MERRA (3DVAR, 2009).

3.3 Climate models

3.3.1 EC Earth

The EC Earth (ECE) 1-degree TCWV dataset has been obtained from atmosphere only global climate model simulations, using prescribed observed sea-surface temperatures and prescribed sea ice for the time period 1979-2008. The ECE global climate model (Hazeleger et al 2010) has been developed from the ECWMF model (<http://eearth.knmi.nl/>). The atmospheric component is based on ECMWF's Integrated Forecasting System (IFS), cycle 31r1 with some additional implementation, including a new convection scheme and the new land surface scheme H-TESSSEL. Small changes in the gravity wave drag and shortwave radiation parameterisations have also been applied to reproduce the observed climatology of the past 40 years as closely as possible and to achieve a balanced radiation budget.

For this study the model was run at T159 (125km) horizontal spectral resolution with 62 vertical levels.

⁵ <http://www.ecmwf.int/en/forecasts/datasets/era-interim-dataset-january-1979-present> (URL tested: 2014-09-05)

3.3.2 MPI-ESM

The Earth System Model of the Max Planck Institute for Meteorology (MPI-ESM) couples atmosphere, ocean and land surface through the exchange of energy, momentum, water, and important trace gases such as carbon dioxide. It has been used for comparative model calculations in the context of CMIP5, which constitute the German contribution to the Fifth Assessment Report of the IPCC (Intergovernmental Panel on Climate Change). It is based on the components of ECHAM6 for the atmosphere and MPIOM for the ocean as well as JSBACH for the terrestrial biosphere and HAMOCC for the ocean's biogeochemistry. The coupling of atmosphere and land on the one hand and ocean and biogeochemistry on the other hand is made possible by the separate coupling program OASIS3. Energy, momentum, water and CO₂ are exchanged with the help of this coupling. Further details and evaluation results can be found in Müller et al. (2012) and Pohlmann et al. (2013).

For this study, we used output from AMIP type simulations using observational based sea surface temperature (SST) and sea ice boundaries (Stevens et al., 2013) in low resolution at 1.875°.

3.4 Climate indices

The above TCWV datasets were evaluated against a variety of climate indices which are described in detail in Table 1 and plotted in Figure 1. The common time period for all datasets is highlighted in grey in Figure 1.

Table 1: Climate Indices used in this study.

Index	Description	Reference	Source
NINO34	El Nino Southern Oscillation Index 3.4. Average sea surface temperature anomaly in the region between 5°N and 5°S as well as 170°W and 120°W.	Rasmusson and Carpenter (1982) Walker (1924)	http://www.esrl.noaa.gov/psd/data/climateindices/list/
PDO	Pacific Decadal Oscillation. The PDO is defined as the leading principal component of North Pacific monthly sea surface temperature variability (pole ward of 20N for the 1900-93 period).	Mantua et al. (1997) Zhang et al. (1997)	http://jisao.washington.edu/pdo/
AO	Arctic Oscillation. The daily AO index is constructed by projecting the daily (00Z) 1000mb height anomalies pole ward of 20°N onto the loading pattern of the AO.	Thompson and Wallace (1998)	http://www.cpc.ncep.noaa.gov/products/precip/CWlink/daily_ao_index/ao.shtml
NAO	North Atlantic Oscillation. The principal component (PC)-based indices of the NAO are the time series of the leading EOF of sea level pressure anomalies over the Atlantic sector, 20°-80°N, 90°W-40°E.	Barnston and Livezey (1987) Hurrell (1995) Rogers (1984) Walker (1924)	https://climatedataguide.ucar.edu/climate-data/hurrell-north-atlantic-oscillation-nao-index-pc-based

Index	Description	Reference	Source
AMM	Atlantic Meridional Mode. The AMM spatial pattern is defined via applying Maximum Covariance Analysis (MCA) to the SST and the 10m wind field over the time period 1950-2005 over the region 21°S to 32°N, and 74° W to 15°E).	Chiang and Vimont (2004)	http://www.esrl.noaa.gov/psd/data/timeseries/monthly/AMM/
AMO	Atlantic Multidecadal Oscillation. The AMO is based upon the average anomalies of SSTs in the North Atlantic basin, typically over 0°N to 80°N.	Schlesinger and Ramankutty (1994)	https://climatedataguide.ucar.edu/search/node/AMO
GHG	Greenhouse gas forcing from NASA GISS	Hansen et al. (2005)	http://data.giss.nasa.gov/modelforce/
SSO2	Stratospheric SO2 forcing from NASA GISS	Hansen et al. (2005)	http://data.giss.nasa.gov/modelforce/
SOL	Solar forcing from NASA GISS	Hansen et al. (2005)	http://data.giss.nasa.gov/modelforce/

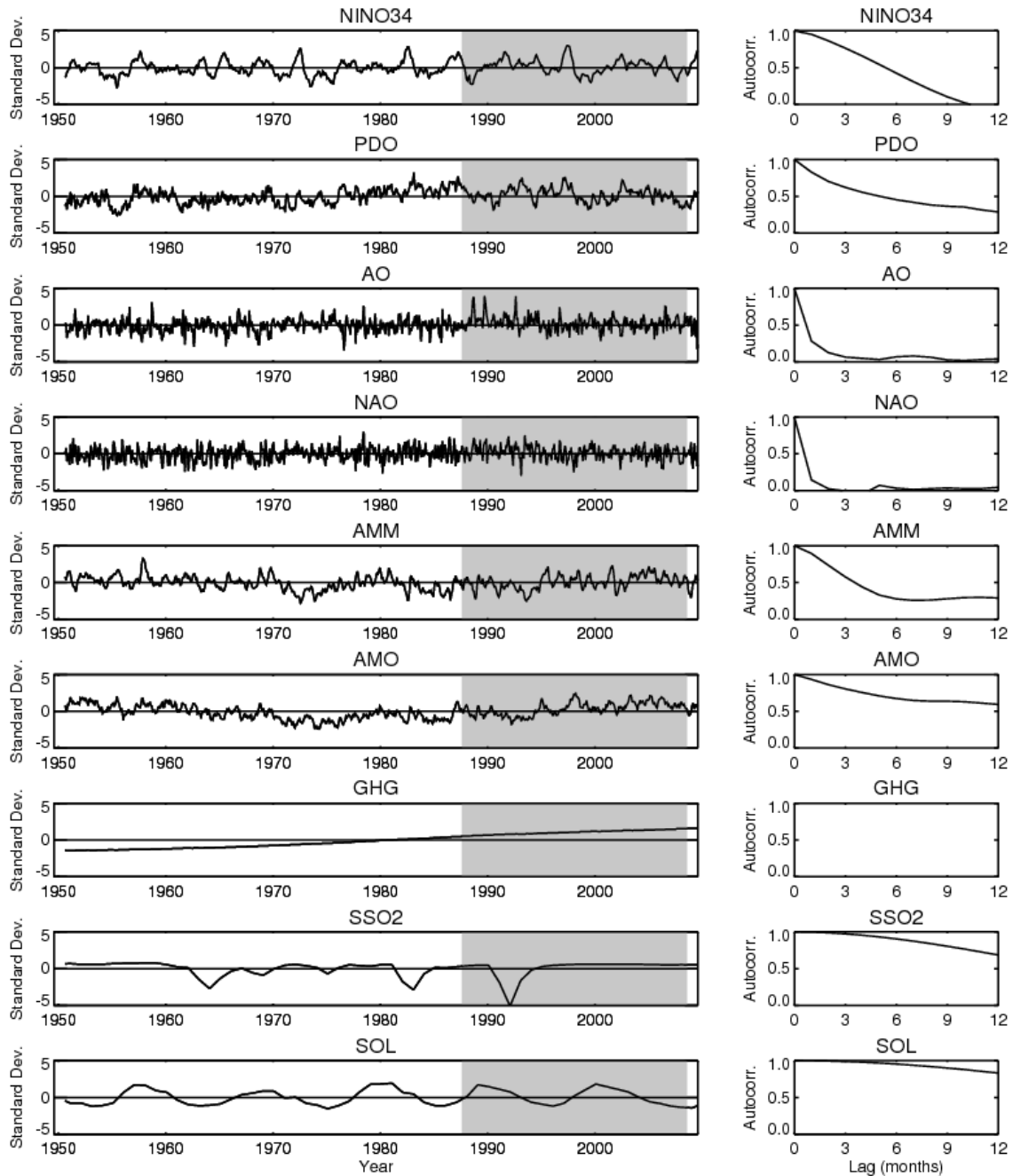


Figure 1: The panels on the left show time series of the different climate indices listed in Table 1. The grey-shaded area in the left panels indicates the 1988-2008 period for which satellite and other water vapour data are evaluated. The right panels show corresponding autocorrelation coefficients for lag times between zero and 12 months.

4 Methods

4.1 Data processing

The analysis is carried out on a common grid and time period. The common grid was defined as a regular longitude/latitude grid with a resolution of $1^\circ \times 1^\circ$ and centre location of the grid boxes between the full degree values, which leads to an array size of 360×180 pixels.

ECE, NVAP-M and RSS were already provided at 1° spatial resolution and thus didn't need to

be remapped. ERA-Interim were available at an array size of 360×181 pixels, which let us assume that latitude grid box midpoints were defined at full degree values. We decided to shift the entire array half degree south by deleting first array line to avoid additional extensive interpolation.

The other four datasets (ESM, HOAPS, CFSR and MERRA) were re-gridded from their native resolutions. The ESM dataset has a spatial resolution of $1.875^\circ \times 1.875^\circ$ with an array size of 192×96 . HOAPS data are provided at a resolution of $0.5^\circ \times 0.5^\circ$ between 80°S and 80°N which leads to an array size of 720×320 . CFSR and MERRA data have resolutions of $0.5^\circ \times 0.5^\circ$ (720×361) and $2/3^\circ \times 0.5^\circ$, respectively (540×361) with latitude grid box midpoints defined similarly to ERA-Interim starting at full values. These dataset were gridded to the common $1^\circ \times 1^\circ$ grid by linear interpolation with shifting the array 0.25° latitude towards South for CFSR and MERRA.

The common period is defined the period jointly covered by all datasets which is the period between 1988 and 2008. We also processed data outside the above defined common period; for example, ERA-Interim, ESM, CFSR, and MERRA data have been processed from 1979 onward.

Monthly temporal resolution has been chosen for the common dataset. Except NVAP-M, all considered data sets were already available as monthly means. For NVAP-M, monthly means were calculated from the provided daily values.

An inventory of all data products generated in the context of VaKaS is given in Appendix B.

4.2 Statistical significance of correlations

The statistical significance is assessed through temporal autocorrelation between time series (Bartlett, 1935; Dawdy and Matalas, 1964). A temporal autocorrelation will reduce the effective number of degrees of freedom in each dataset. Assuming the autocorrelation processes to be characterized by red noise yields an effective time scale T_0 of independent samples of:

$$T_0 = \frac{1 + r_{1,x} \cdot r_{1,y}}{1 - r_{1,x} \cdot r_{1,y}} \quad (1)$$

In our case, T_0 is given in units of months and $r_{1,x}$ designates the lag-1 autocorrelation for dataset x. More generally, $r_{L,x}$ is the lag-L autocorrelation for dataset x with L being the time shift in months. The corresponding autocorrelation coefficients for dataset y are denoted analogously.

For an arbitrarily auto-correlated variable, the equivalent formula is:

$$T_0 = 1 + 2 \sum_{L=1}^N \left(1 - \frac{L}{N}\right) r_{L,x} \cdot r_{L,y} \quad (2)$$

The independent sample size is then given as:

$$N_{\text{eff}} = \frac{N}{T_0}, \quad (3)$$

with N being the number of months in the time series ($N=720$ for the 60-years' time series shown in Figure 1, $N=252$ for the satellite time series 1988-2008). The correlation coefficient required to exceed the 95 % significance level is shown in Figure 2 as function of N_{eff} .

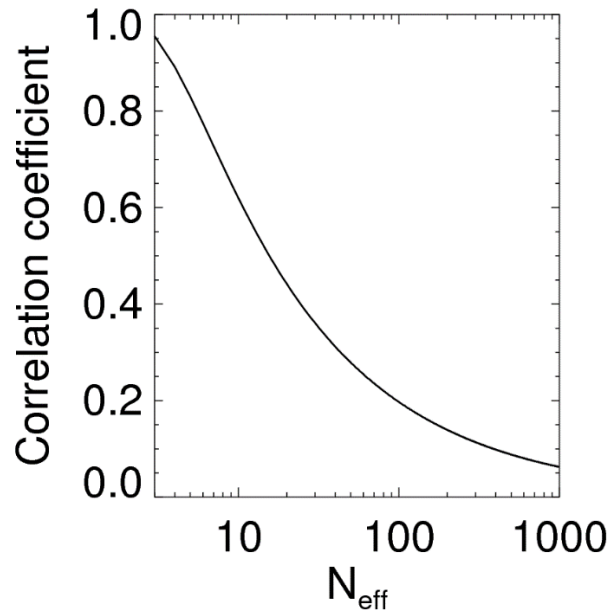


Figure 2: Absolute correlation coefficients corresponding to a 95% statistical significance level as function of effective sample size N_{eff} . Data are produced using a two-sided t-test. These values are used throughout this paper to assess the statistical significance of time series correlations with N_{eff} calculated from Equations (2) and (3) for arbitrary temporal autocorrelations and Equations (1) and (3) for red noise, respectively.

A few issues to note in the analysis and discussion of correlation coefficients and their significance:

- All climate indices and water vapour fields were corrected for seasonal effects by subtracting from each monthly data point the long-term average over that month. We are thus interpreting monthly anomaly fields throughout this paper.
- We are using two-sided t-tests, i.e. we are assuming the sign of the correlation to be unknown. This yields the most stringent significance criteria although in some cases one could argue the correlation has to have a certain sign.
- We restrict most of the discussion below to red noise (Equation (1)) but do also provide results for the actual autocorrelation functions (Equation (2)) in Appendix A. The differences between both cases are mostly marginal and do not affect our findings.
- The lower the temporal autocorrelation of a particular variable, the lower the correlation coefficient can be between that variable and any other variable without losing statistical significance. This is because the effective number of observations N_{eff} will remain high by virtue of the product of the lag-1 autocorrelations showing up in Equation (1), respectively. Thus, if only one variable exhibits pure white noise, then $N = N_{\text{eff}}$ regardless of how highly auto-correlated the second variable is.
- A statistically significant correlation coefficient does not necessarily imply causal or physical relation between two datasets (“correlation does not imply causation”).

5 Results

5.1 Statistical assessment of climate indices

In this section we assess the different climate indices outlined in Table 1 statistically with respect to the following questions:

1. To what extent are the different climate indices independent of each other?
2. All climate indices used herein go back at least until 1951. How similar is the period 1988-2008 for which we have water vapour observations to the 60-years period 1951-2010?

To answer the first question we performed statistical significance tests on the correlation between different indices. The comparison was done on monthly anomalies which were normalized to zero mean and unit standard deviation. The resulting time series are shown in Figure 1. With the exception of AO and NAO, the lag-1 autocorrelation of the time series is 0.9 or higher and clearly none of the time series exhibits a pure white noise behaviour (which would result in a lag-1 autocorrelation of zero). Thus, in most cases the effective sample size is significantly lower than the actual sample size.

The correlation coefficients between the different climate indices are shown in Figure 3. The variance explained by regressing y against x is equal to r^2 . Since the resulting standard deviations for any two datasets x and y are unity, the correlation coefficient r is identical to the regression slope between the two datasets. Performing a two-sided t-test on the datasets yields the statistically significant correlations highlighted bold in Figure 3. The t-test was performed assuming red noise, i.e. modelling the effective sample size according to Equations (1) and (3). As outlined above, these estimates are likely conservative in that a red noise (Markov) auto-correlative process is assumed, which likely underestimates the degrees of freedom in the dataset.

In the longer time series, significant correlations occur between various tuples of variable, including (PDO, NINO34) and (AO, NAO, AMM, AMO). NAO is closest to a white noise process with a very low lag-1 autocorrelation. Thus, the correlation between NAO and any other variable are more likely to be statistically significant because of a relatively high N_{eff} as outlined in Section 4.2.

Additionally, high correlations are found between AMM, AMO, SSO2, and GHG. Note, that GHG closely resembles a linear trend. The correlations between (SSO2, GHG) and (AMO, AMM) are less pronounced in the longer data set.

To assess the representativeness of the shorter time period with respect to the longer period, we show in the lower left panel of Figure 3 the difference between the correlation coefficients for the short and long time series (i.e. the difference between the values shown in the upper right and upper left panels of Figure 3). The underlying colours show exactly the difference in correlation coefficient whereas the numerical values show the ratio of the two correlation coefficients in percent.

For the pair (PDO, AO), this ratio is 181% which results from the correlation coefficient between the two indices being -0.3 for the short time series but only -0.164 for the long time series. This ratio can be interpreted as follows: Even though in both, the short and the long time series the correlation between PDO and AO is statistically significant, the correlation coefficients are different with the correlation coefficient being 81% larger in the short time series than in the long time series, thus PDO explains $1.812 = 3.52$ times more variance in AO in the short time series than in the long time series. Also, since both time series are normalized, the correlation coefficients are identical to the slopes of the regression lines between the two datasets. Therefore, again for the case (PDO, AO), the slope of a regression between the two datasets is a factor of 1.81 different between the short and the long time series.

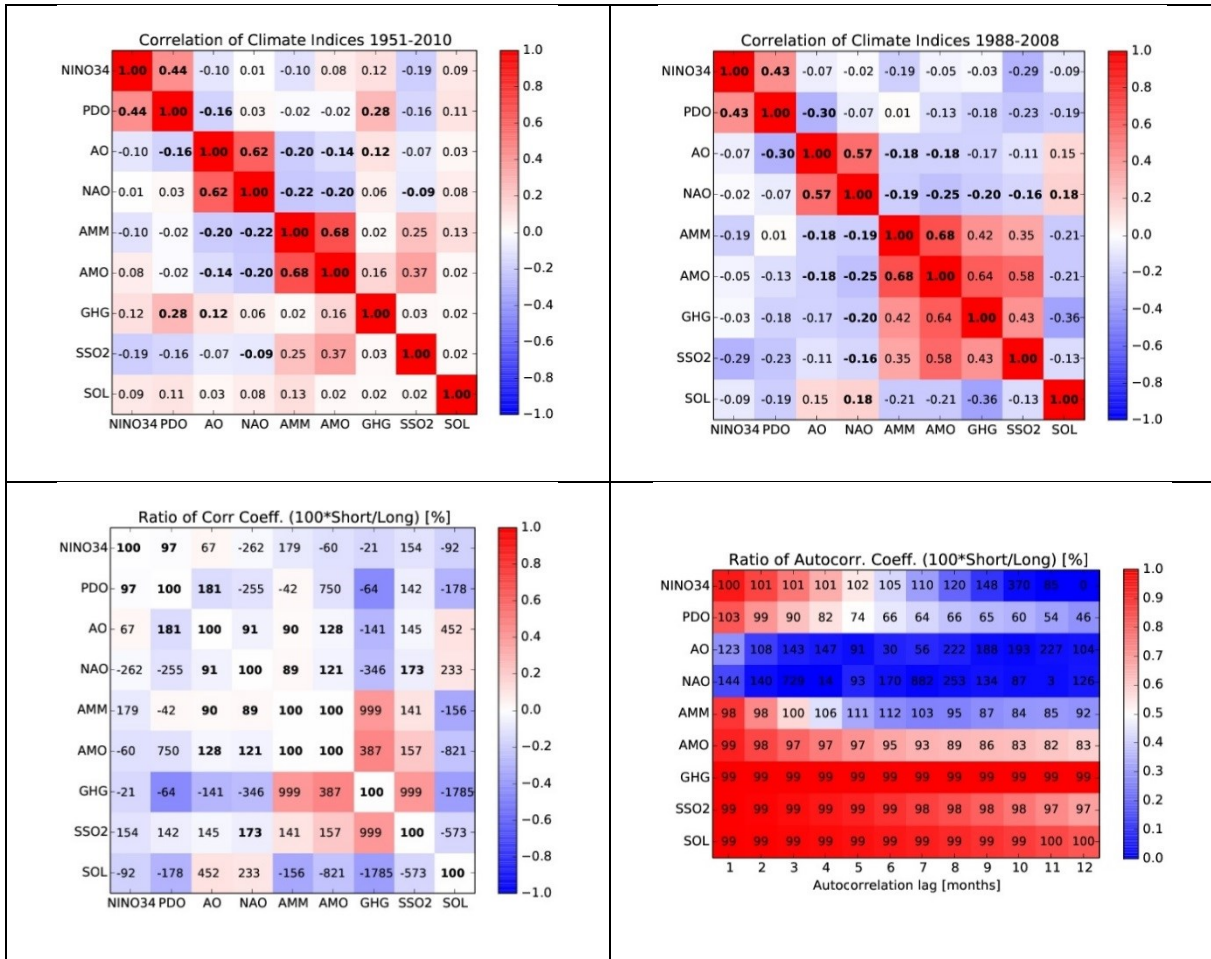


Figure 3: The upper left panel provides the correlation coefficients between the different climate indices listed in Table 1 for the 60-years period 1951-2010. The upper right panel shows the same statistics for the period 1988-2008. Correlation coefficients that are statistically significant at the 95% level assuming red noise are highlighted bold. The lower left panel shows the differences in correlation coefficients between the short and the long time series (colours) and ratio between those correlation coefficients (numbers) with only those coefficients highlighted bold that are statistically significant in both the short and the long time series. The values for the lower left panel are given in percentage amounts capped at 999%. A value of 999 thus indicates a difference in correlation coefficient between the short and long time series of a factor 9.99 or higher (e.g. correlation short of 0.6, correlation long of 0.05). The lower right plots shows ratios in lagged autocorrelations between the short and the long times series as function of autocorrelation lag. The background is the autocorrelation coefficient for the long time series, which is also plotted in Figure 1 (right panels).

These results allow to further narrow down the number of stably cross-correlated datasets. Setting an ad-hoc criterion of a valid range in the ratio of correlation coefficients to 70%-130%, we find that only the pair (NINA34, PDO) and the tuple (AO, NAO, AMM, AMO) are statistically significantly correlated in both the long and the short time series and their correlation coefficient is sufficiently similar ($\pm 30\%$).

A similar analysis can be performed on the lag-L autocorrelation coefficients for each time series and is shown in Figure 3, lower right panel. For example, the value of 144% for NAO at lag-1 indicates that the lag-1 autocorrelation coefficient in the short time series is a factor of 1.44 higher than for the long time series. With the exception of NAO and, to a lesser extent,

AO, the autocorrelation functions of the different indices are rather similar between the long and the short time series: up to lag-5 the autocorrelation functions between the short and long time series do not differ by more than $\pm 30\%$. As pointed out further up, AO and NAO exhibit very weak temporal autocorrelations (i.e. they behave more like white noise). Therefore, lower stability of the autocorrelation function is to be expected.

In summary, significant and stable correlations exist between the pair (NINA34, PDO) and the tuple (AO, NAO, AMM, AMO). AO and NAO show a very different behaviour from the rest of the indices, in that these two indices exhibit more of a random behaviour than the other indices, which are relatively highly temporally auto-correlated. GHG, SSO2, and SSOL exhibit a strongly auto-correlated behaviour. GHG resembles a linear trend thus having approximately zero degrees of freedom. SSOL is a cyclical function with frequency of the solar cycle (11 years)⁻¹.

5.2 Analysis of water vapour datasets

The analysis in Section 5.1 highlights the strong correlation between ENSO and TCWV. This result is corroborated by Figure 4, where the first four temporal Eigenvectors of ERA-Interim are compared to NINO34 for the time period 1988 to 2008. One can see the excellent agreement between the first Eigenvector and the NINO34 time series.

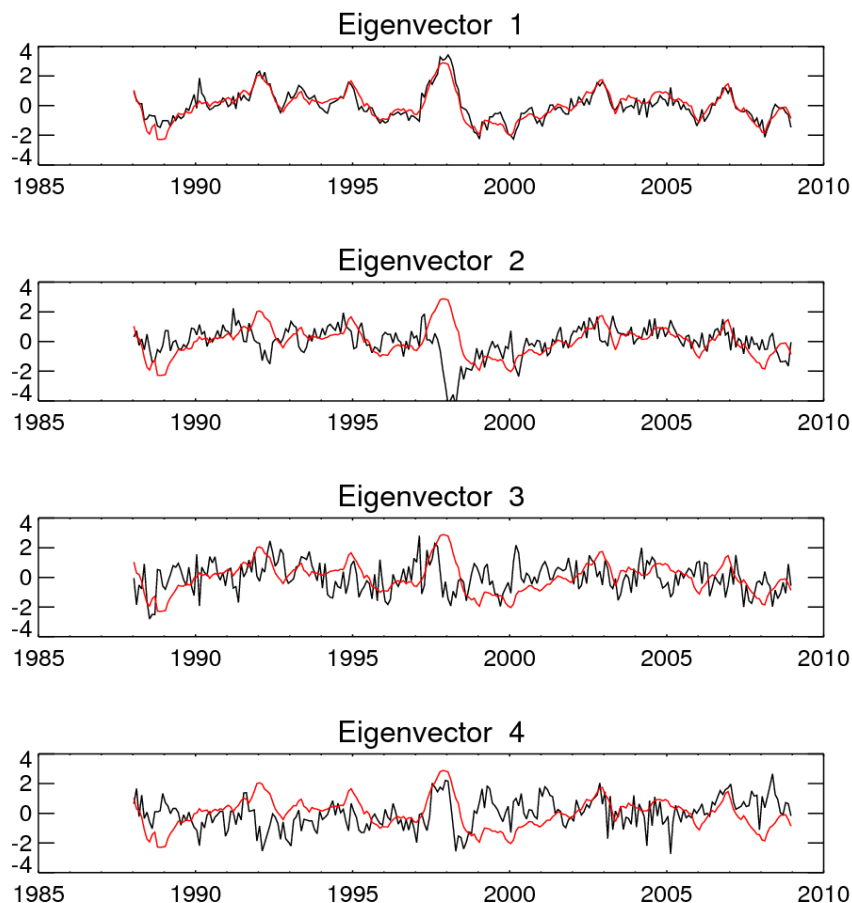


Figure 4: First four temporal eigenvectors of the ERA-Interim TCWV (black curves). The red curve shows NINO34 values for comparison. All curves are normalized to zero mean and unit standard deviation for visualization. The variance explained by the first four eigenvectors is 12.7%, 6.1%, 3.4%, and 3.1%, respectively.

Figure 5 shows the empirical orthogonal functions (EOFs) associated with the Eigenvectors shown in Figure 4.

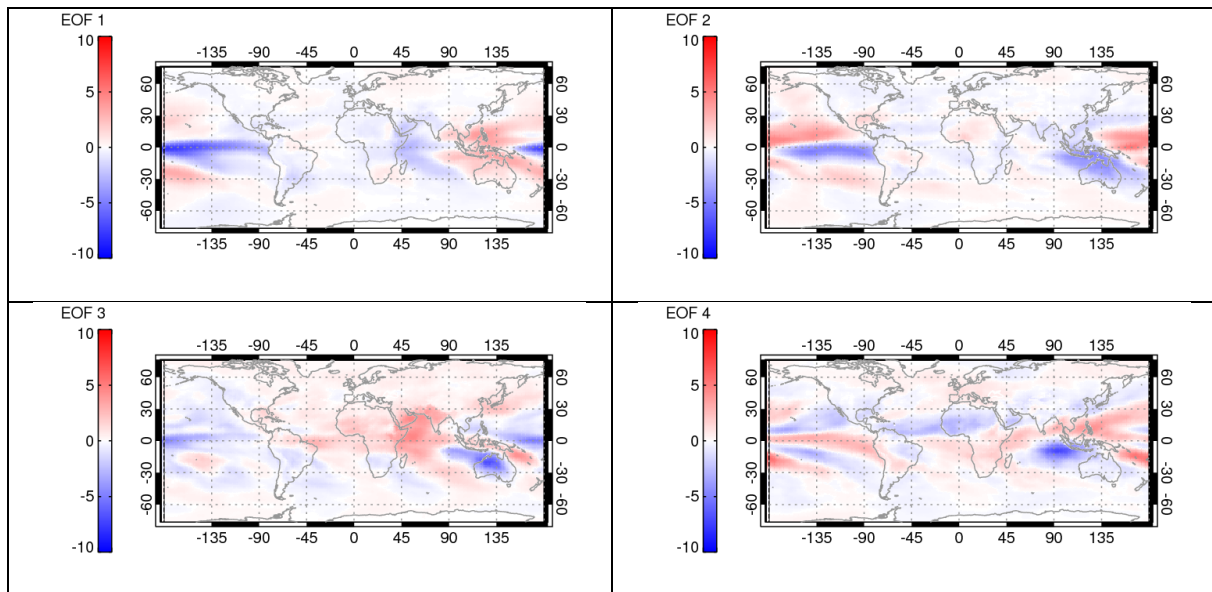


Figure 5: First four EOFs for ERA-Interim TCWV associated with the eigenvectors shown in Figure 4. EOFs are shown normalized by the square root of their respective eigenvalue (yielding units of kg/m² for the EOFs).

Table 2 shows the correlations between the NINO34 time series and the first Eigenvector of each of the TCWV datasets. Results are shown for all surfaces and, separately, for ocean only.

Table 2: Correlation of the first EOF of different TCWV datasets with NINO34. The column labelled 'All' shows correlations for the entire datasets including ocean, land, and ice - if included in the dataset. The column 'Ocean' shows the correlations for ocean data points that are ice-free over the entire period.

Dataset	Correlation with NINA34	
	All	Ocean
RSS	0.893	0.893
HOAPS	0.895	0.895
NVAP-M	0.752	0.864
ERA-Interim	0.895	0.889
MERRA	0.898	0.891
CFSR	0.879	0.869
ECE	0.899	0.908
ESM	0.884	0.903

It is noteworthy that all datasets show very similar correlation coefficients to NINO34 everywhere, except for NVAP-M, which shows systematically lower correlation coefficients with ENSO (NINO34) if land is included. This result will require further analysis and might be related to the particular retrieval algorithms used in NVAP-M for TCWV retrievals over land surfaces. An indication for this hypothesis is given in the lag-1 autocorrelation, which is

unusually high over desert areas as well as Antarctica (see Appendix, Figure 17). The two climate models ECE and ESM show results very similar to the other datasets.

Figure 6 shows correlation results for ERA-Interim against all climate indices as an example. Areas exceeding the 95% significance level for red noise are highlighted with thick grey lines. Figure 13 to Figure 19 in Appendix A provide analogous information for all other TCWV datasets for red as well as for white noise.

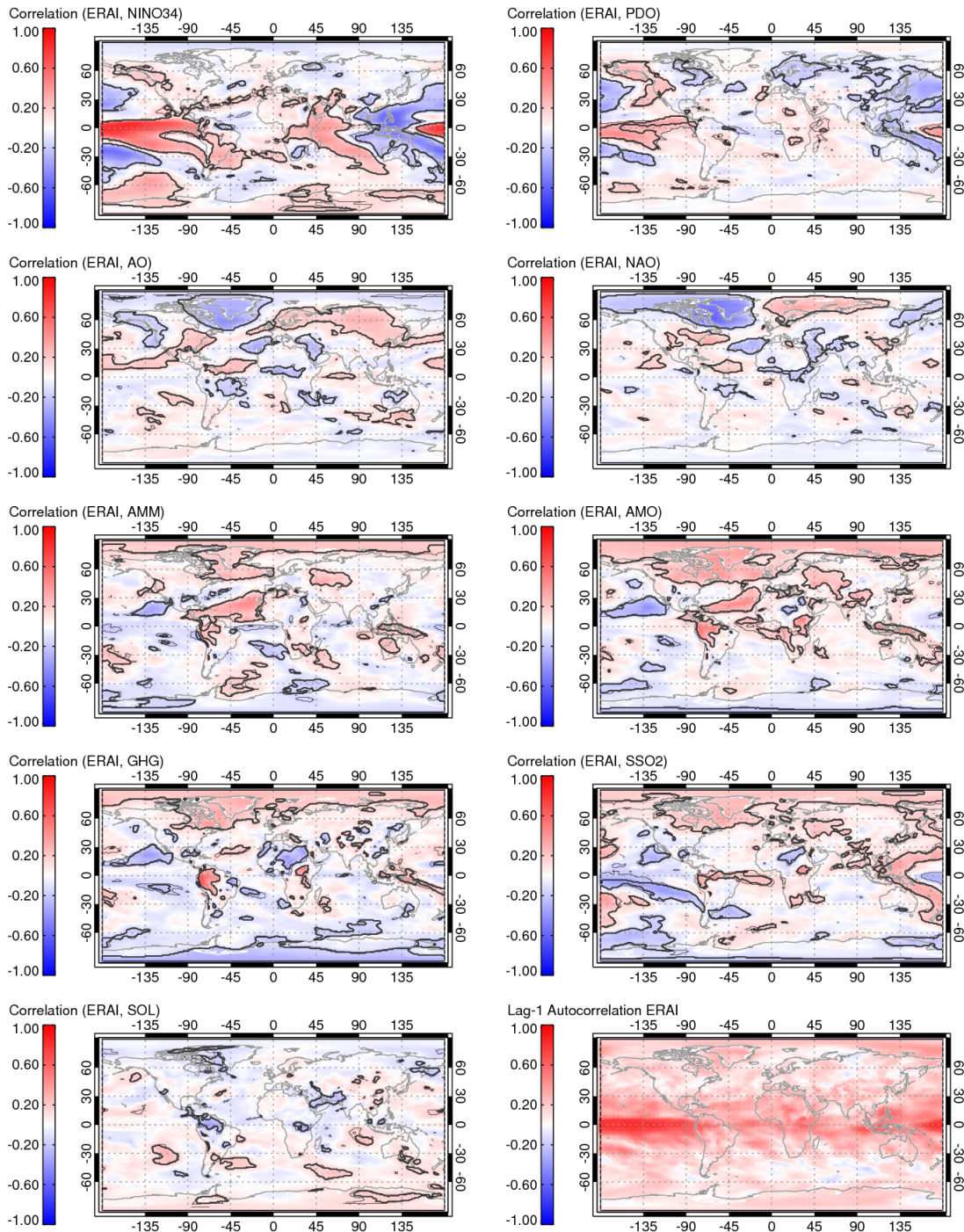


Figure 6: Correlation between various climate indices and ERA-Interim TCWV. Thick grey isolines show areas with correlations exceeding the 95% significance level for red noise. These occur only for NINO34, PDO, AO, and NAO. Thin grey lines show 95% confidence levels for white noise. The panel on the lower right shows the lag-1 autocorrelation of ERA-Interim.

A merged view over all datasets is shown in Figure 7 highlighting those areas where all resp. more than half of the datasets show statistically significant correlations with the different climate indices.

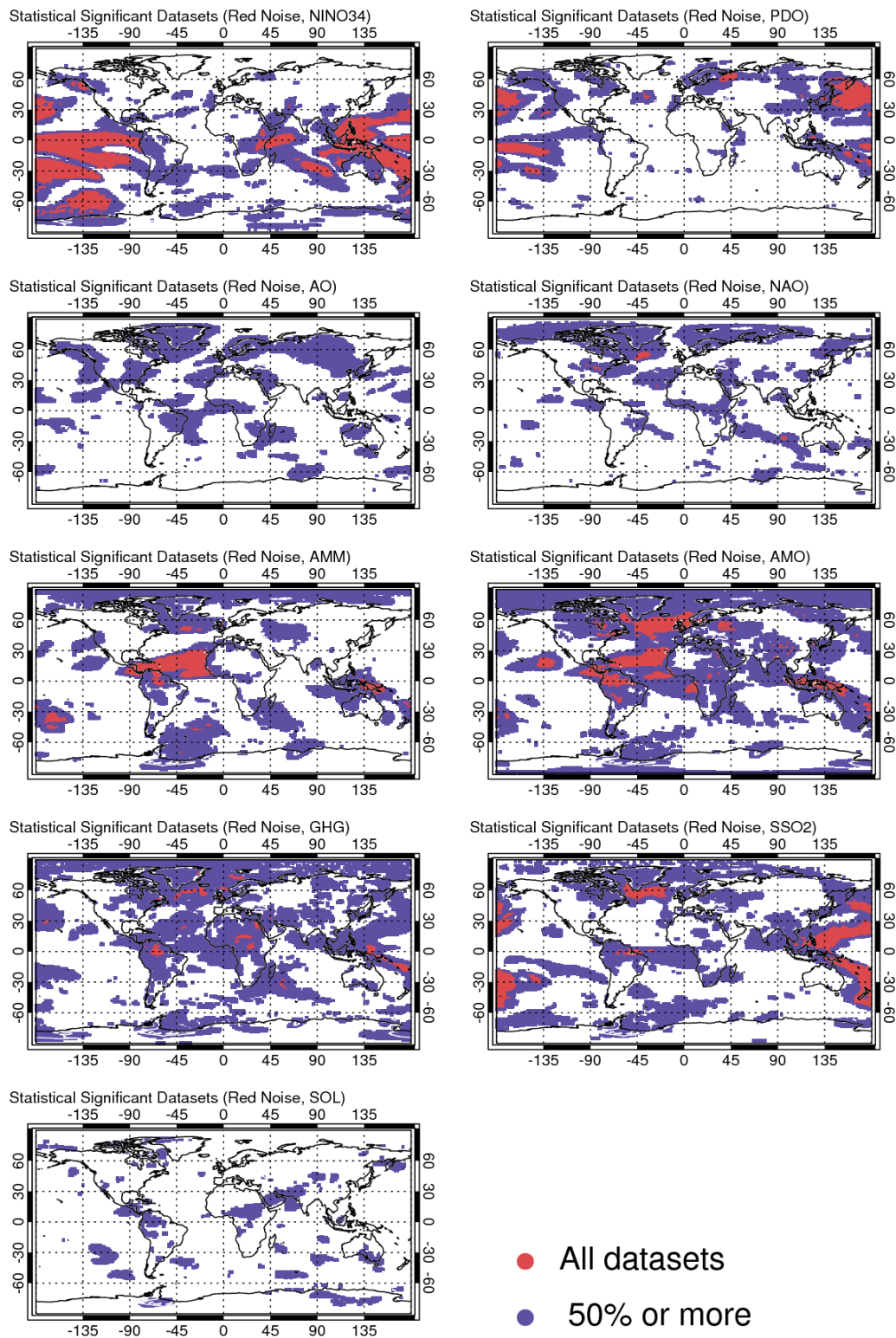


Figure 7: These plots provide a summary of where the different TCWV datasets significantly correlate with the various climate indices (assuming red noise, i.e. using Equation (1) to calculate N_{eff}). Regions where at least half of the datasets show significant correlations with a given climate index are highlighted blue. Regions where all datasets show significant correlations are highlighted red.

As expected from the above correlation analysis, the largest areas of coherent correlations include the tropical Pacific for NINO34 and the northern Pacific Ocean for PDO. AMM shows a larger area in the northern tropical and subtropical Atlantic with high correlations for all TCWV datasets. AMO shows large areas of statistically significant correlations against all TCWV datasets for that same area as well as for the northern Atlantic. Finally, all datasets are significantly correlated with stratospheric SO₂ loading for two tongues stretching out into the northern and southern Pacific as well as for the northern Atlantic. AO, NAO, GHG, and SOL show only very small areas with consistent correlations, if any. A detailed analysis of the correlation maps provided for ESM and ECE (Appendix, Figure 18 and Figure 19) shows them to be very similar to the other datasets.

5.3 Assessment of ECE and ESM versus other datasets

ECE and ESM operated in a ‘climate-mode’ in which only sea ice, sea surface temperatures, and external forcings are prescribed. With those lateral boundary conditions the model is allowed to develop freely. In addition to these boundary conditions, reanalysis dataset (MERRA, CFSR, and ERAI) also assimilate atmospheric observations thereby providing an analysis of the actual state of the atmosphere at any given time. Similarly, the observational datasets (RSS, HOAPS, and NVAPM) provide estimates of the actual state of the atmosphere. Therefore, one can expect the reanalysis and observational datasets to also represent the synoptic situation at any given time, while the two climate-mode models cannot be expected to provide any information about the actual synoptic situation.

Contrasting ESM and ECE against the other models might therefore help understand to what degree TCWV climatologies are affected by ‘weather’ as opposed to climatological boundary conditions such as external forcings and SST. Figure 8 provides the same information as Figure 7, but is restricted to observational and reanalysis datasets, thus excluding ESM and ECE. Comparing Figure 8 to Figure 7, one can see that the inclusion of ECE and ESM reduces the areas of agreement between all datasets (less red areas in Figure 7). This effect is particularly strong for AO and NAO, with which ESM and ECE show only very weak correlations (see also Figure 18 and Figure 19). This result is not surprising as AO and NAO are derived from surface pressure fields whereas e.g. PDO, NINO34, and AMM are derived from SST fields. Surface pressure is of course intimately connected to weather. Because the two climate-mode models are not capable of reproducing weather patterns, it appears unlikely they would correlate well with climate indices relying on surface pressure. In contrast, sea surface temperature fields are prescribed for all models. To the extent in which SST affects TCWV, ECE and ESM should thus react similar to the reanalysis datasets. A similar effect can be seen for GHG and, to a lesser extent for SOL.

While Figure 7 and Figure 8 indicate areas with statistically significant correlations for all datasets, these are not separated by positive versus negative correlations. Figure 9 and Figure 10 are similar to Figure 8 but separate areas with positive and negative correlations. Comparing Figure 9 and Figure 10, it becomes clear that for AMO, AMM, GHG and SSO₂ agreements between the TCWV datasets occur almost only for positive correlations. In contrast, ENSO, PDO, AO, and NAO show areas of positive and negative correlations. Thus, in a strongly positive ENSO certain regions get moister whereas others get drier agreeably between all datasets. In contrast, in a strongly AMM state, all datasets agree the tropical and subtropical northern Atlantic gets wetter, but except for a small area in the north-eastern Pacific, there is no agreement between models which areas get drier (if any).

Figure 11 shows the anomaly time series correlation between all indices and all TCWV datasets for all areas where the datasets agree on positive correlations (Figure 11, left panel) and negative correlations, respectively (Figure 11, right panel). In those areas, where all datasets agree on a significant positive correlation with ENSO, MERRA and NVAPM show the lowest correlation

(0.73 and 0.79, respectively). ECE and ESM show significantly lower positive correlations with AO, NAO, and SOL compared to the other datasets. For the negatively correlated areas a very similar picture arises with ESM and ECE less strongly correlated with AO and NAO. In addition also AMM and AMO and SSO2 show less strong negative correlations with ESM and ECE for the negatively correlated areas.

In summary:

- For the climate indices built on atmospheric parameters (AO, NAO), ECE and ESM show much weaker correlations than all other models. This is perhaps not surprising since the ESM and ECE are allowed to freely form their own ‘weather’.
- For the climate indices built on SST (NINO34, PDO, AMM, AMO), the two climate-mode models perform very similar to the other models and datasets especially in positively correlated areas.
- For the forcing indices (SOL, GHG, and SSO2) ECE and ESM show slightly lower correlations than the other datasets but results are not consistent. It is unclear what the origin of the reduced correlation is. ECE appears to (Willén, pers. comm.) whereas ESM appears to include GHG, SSO2, and SOL forcings (Stevens et al., 2013).

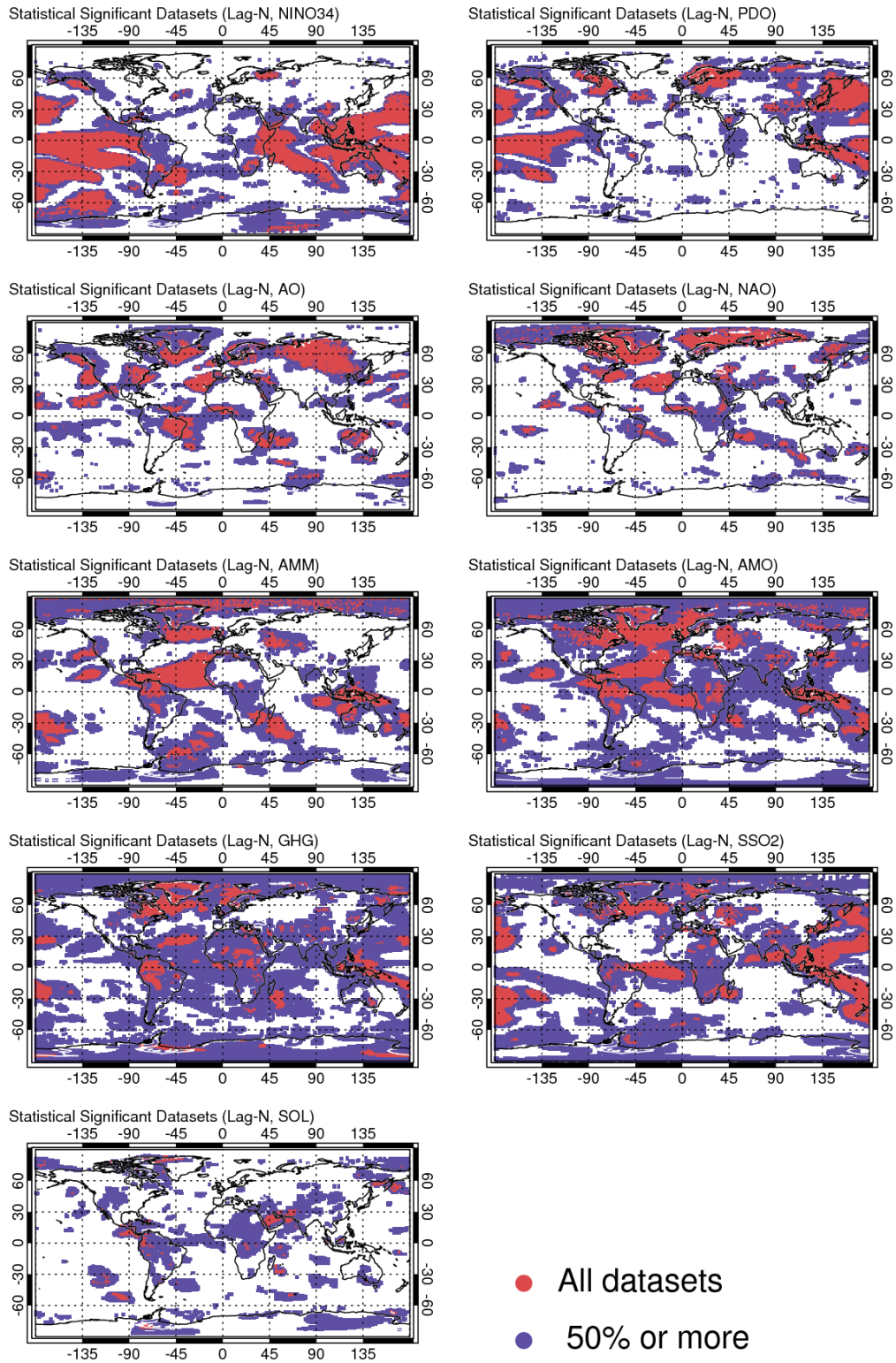


Figure 8: Same as Figure 7 but excluding ESM and ECE.

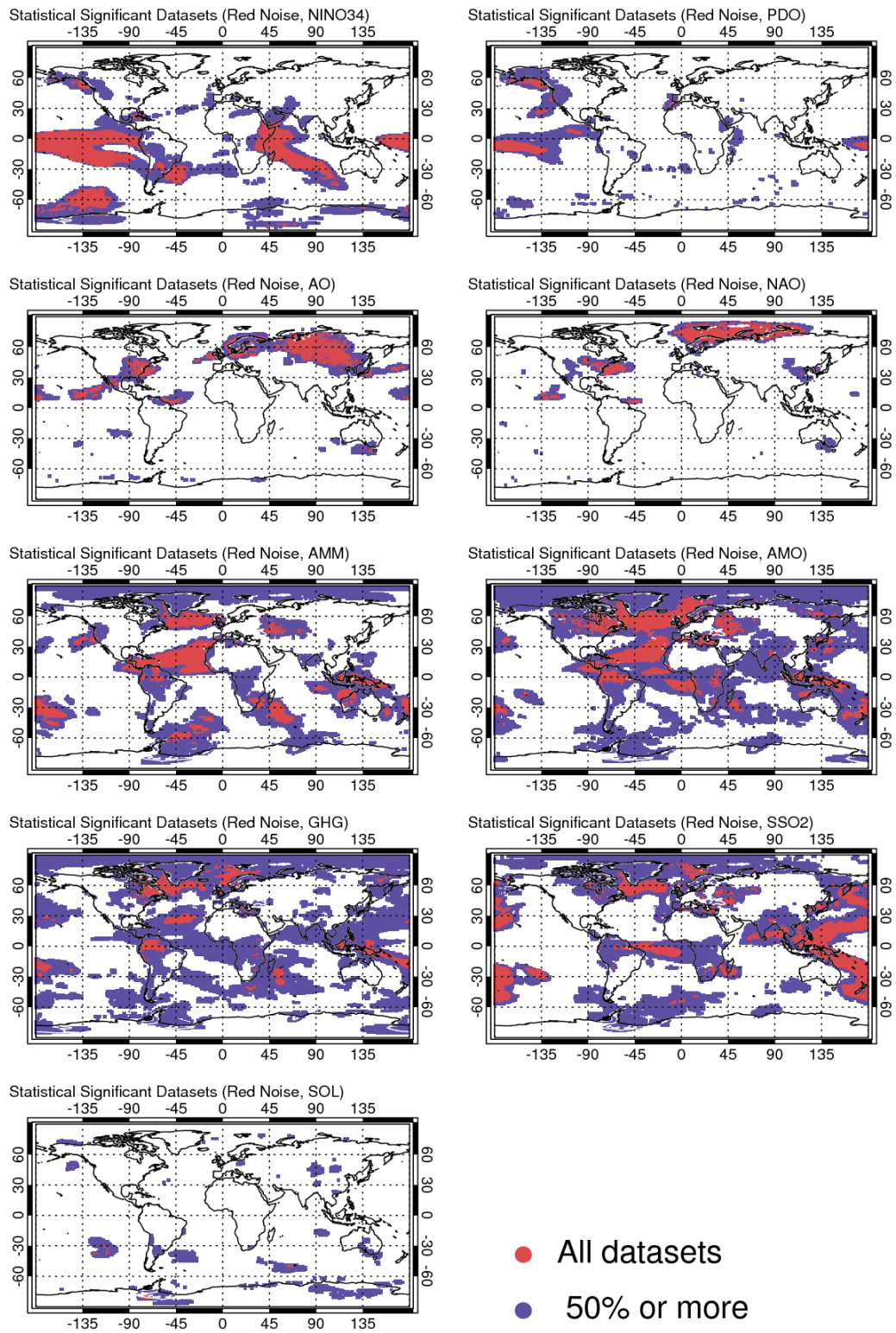


Figure 9: Same as Figure 8, but only for areas where the correlation between indices and water vapour datasets is positive.

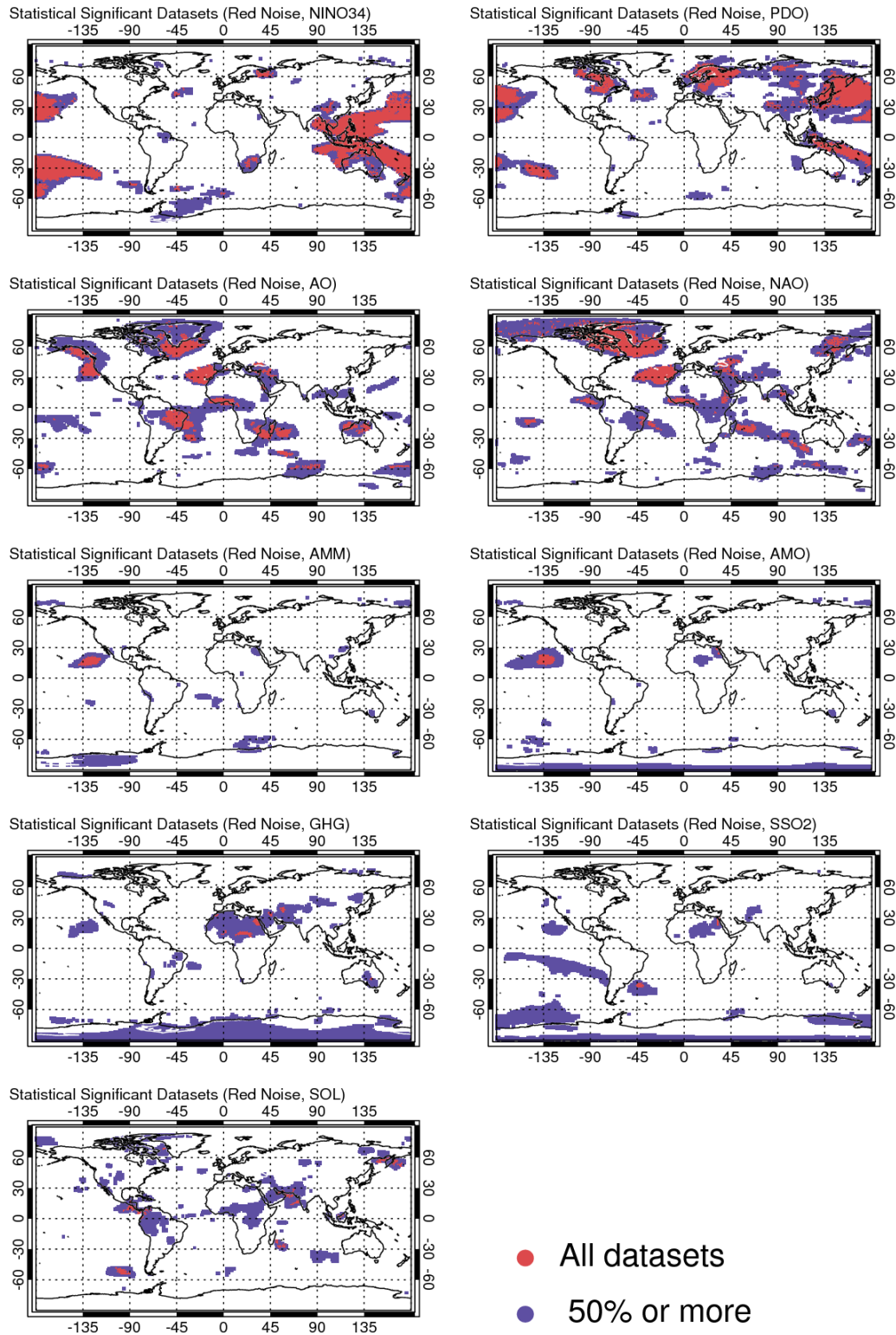


Figure 10: Same as Figure 8, but only for areas where the correlation between indices and water vapour datasets is negative.

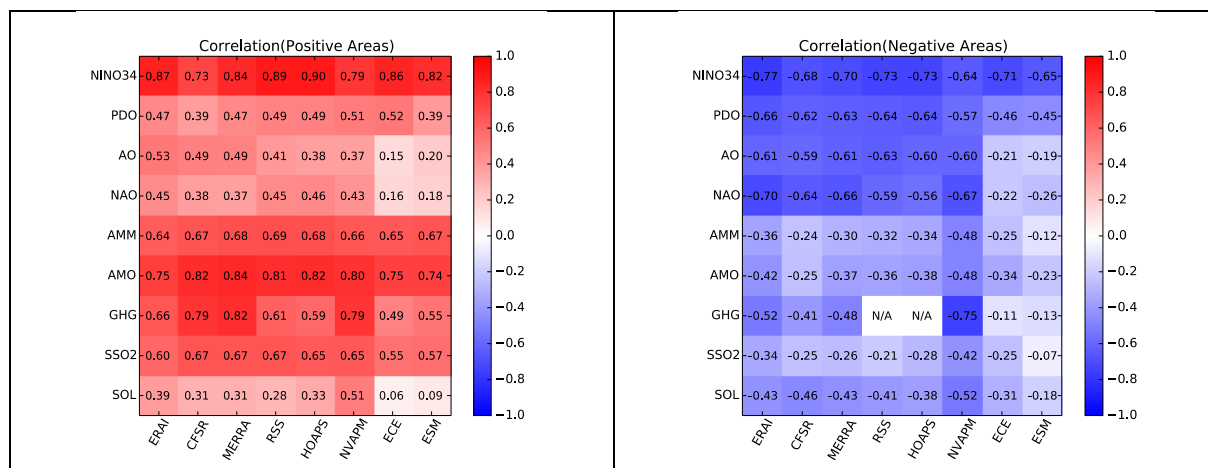


Figure 11: The left panel shows correlation between climate indices and TCWV datasets for regions where all datasets show a significant positive correlation (red areas in Figure 9). The right panel shows the same for negative correlations (red areas in Figure 10). For the two correlations marked 'N/A' no data points exist because the two datasets are only defined over land but all red areas for GHG in Figure 10 are over land.

6 Conclusions

Eight TCWV datasets were analysed and compared to nine climate indices. All datasets are highly correlated with ENSO and show different levels of correlation with other climate indices. The two climate models ESM and ECE do not differ significantly from the other datasets, all of which either retrieve or assimilate water vapour information directly.

7 References

- Andersson, A., C. Klepp, K. Fennig, S. Bakan, H. Grassl, and J. Schulz (2011), Evaluation of HOAPS-3 Ocean Surface Freshwater Flux Components, *J Appl Meteorol Clim*, 50(2), 379-398, doi: 10.1175/2010jamc2341.1.
- Barnston, A. G., and R. E. Livezey (1987), Classification, Seasonality, and Persistence of Low-Frequency Atmospheric Circulation Patterns, *Mon. Wea. Rev.*, 115, 1083-1126.
- Bartlett, M. S. (1935), Some aspects of the time-correlation problem in regard to tests of significance, *J. Roy. Stat. Soc.*, 98, 536-543.
- Chiang, J. C. H., and D. J. Vimont (2004), Analogous meridional modes of atmosphere-ocean variability in the tropical Pacific and tropical Atlantic, *J. Climate*, 17(21), 4143-4158.
- Dawdy, D. R., and N. C. Matalas (1964), Statistical and probability analysis of hydrologic data, Part III: Analysis of variance, covariance and time series, in *Handbook of Applied Hydrology*, a Compendium of Water-Resources Technology, edited by V. T. Chow, pp. 8.68-68.90, McGraw-Hill Book, New York.
- Dee, D. P., Uppala, S. M., Simmons, A. J., Berrisford, P., Poli, P., Kobayashi, S., Andrae, U., Balmaseda, M. A., Balsamo, G., Bauer, P., Bechtold, P., Beljaars, A. C. M., van de Berg, L., Bidlot, J., Bormann, N., Delsol, C., Dragani, R., Fuentes, M., Geer, A. J., Haimberger, L., Healy, S. B., Hersbach, H., Hólm, E. V., Isaksen, L., Kállberg, P., Köhler, M., Matricardi, M., McNally, A. P., Monge-Sanz, B. M., Morcrette, J.-J., Park, B.-K., Peubey, C., de Rosnay, P., Tavolato, C., Thépaut, J.-N., and Vitart, F. (2011), The ERA-Interim reanalysis: configuration and

performance of the data assimilation system. *Q.J.R. Meteorol. Soc.*, 137: 553–597. doi: 10.1002/qj.828.

Hansen, J., M. Sato, R. Ruedy, L. Nazarenko, A. Lacis, and G. A. Schmidt (2005), Efficacy of climate forcings, *Journal of Geophysical Research*, 110(D18), doi: 10.1029/2005jd005776.

Hazeleger, W., Severijns, C., Semmler, T., Stefanescu, S., Yang, S., Wang, X., Wyser, K., Dutra, E., Baldasano, J. M., Bintanja, R., Bougeault, P., Caballero, R., Ekman, A. M. L., Christensen, J. H., van den Hurk, B., Jimenez, P., Jones, C., Kallberg, P., Koenigk, T., McGrath, R., Miranda, P., van Noije, T., Parodi, J. A., Schmith, T., Selten, F., Storelvmo, T., Sterl, A., Tapamo, H., Vancoppenolle, M., Viterbo, P., and Willén, U., 2010: EC-Earth: A Seamless Earth-System Prediction Approach in Action, *Bull Amer Meteor Soc*, 91, 1357-1363.

Hilburn, K. A., and F. J. Wentz (2008), Intercalibrated Passive Microwave Rain Products from the Unified Microwave Ocean Retrieval Algorithm (UMORA), *J Appl Meteorol Clim*, 47(3), 778-794, doi: 10.1175/2007jamc1635.1

Hurrell, J. W. (1995), Decadal trends in the North Atlantic Oscillation: Regional temperatures and precipitation, *Science*, 269(5224), 676-679.

Müller, W. A., J. Baehr, H. Haak, J. H. Jungclauss, J. Kröger, D. Matei, D. Notz, H. Pohlmann, J. S. von Storch, J. Marotzke (2012), Forecast skill of multi-year seasonal means in the decadal prediction system of the Max Planck Institute for Meteorology, *Geophysical Research Letters*, 39(22).

Mantua, N. J., S. R. Hare, Y. Zhang, J. M. Wallace, and R. C. Francis (1997), A Pacific Interdecadal Climate Oscillation with Impacts on Salmon Production, *B Am Meteorol Soc*, 78(6), 1069-1079.

Pohlmann, H., W. A. Müller, K. Kulkarni, M. Kameswarrao, D. Matei, F. S. E. Vamborg, C. Kadow, S. Illing, J. Marotzke (2013), Improved forecast skill in the tropics in the new MiKlip decadal climate predictions, *Geophysical Research Letters*, 40(21), 5798–5802.

Rasmusson, E. M., and T. H. Carpenter (1982), Variations in Tropical Sea Surface Temperature and Surface Wind Fields Associated with the Southern Oscillation/El Niño, *Mon. Wea. Rev.*, 110, 354-384

Rienecker, Michele M., Max J. Suarez, Ronald Gelaro, Ricardo Todling, Julio Bacmeister, Emily Liu, Michael G. Bosilovich, Siegfried D. Schubert, Lawrence Takacs, Gi-Kong Kim, Stephen Bloom, Junye Chen, Douglas Collins, Austin Conaty, Arlindo da Silva, Wei Gu, Joanna Joiner, Randal D. Koster, Robert Lucchesi, Andrea Molod, Tommy Owens, Steven Pawson, Philip Pegion, Christopher R. Redder, Rolf Reichle, Franklin R. Robertson, Albert G. Ruddick, Meta Sienkiewicz, and Jack Woollen, 2011: MERRA: NASA's Modern-Era Retrospective Analysis for Research and Applications. *J. Climate*, 24, 3624–3648, doi: <http://dx.doi.org/10.1175/JCLI-D-11-00015.1>.

Rogers, J. C. (1984), An Association between the North Atlantic Oscillation and the Southern Oscillation in the Northern Hemisphere, *Mon. Wea. Rev.*, 112, 1999-2015.

Saha, Suranjana, Shrinivas Moorthi, Hua-Lu Pan, Xingren Wu, Jiande Wang, Sudhir Nadiga, Patrick Tripp, Robert Kistler, John Woollen, David Behringer, Haixia Liu, Diane Stokes, Robert Grumbine, George Gayno, Jun Wang, Yu-Tai Hou, Hui-Ya Chuang, Hann-Ming H. Juang, Joe Sela, Mark Iredell, Russ Treadon, Daryl Kleist, Paul Van Delst, Dennis Keyser, John Derber,

Michael Ek, Jesse Meng, Helin Wei, Rongqian Yang, Stephen Lord, Huug Van Den Dool, Arun Kumar, Wanqiu Wang, Craig Long, Muthuvel Chelliah, Yan Xue, Boyin Huang, Jae-Kyung Schemm, Wesley Ebisuzaki, Roger Lin, Pingping Xie, Mingyue Chen, Shuntai Zhou, Wayne Higgins, Cheng-Zhi Zou, Quanhua Liu, Yong Chen, Yong Han, Lidia Cucurull, Richard W. Reynolds, Glenn Rutledge, and Mitch Goldberg, 2010: The NCEP Climate Forecast System Reanalysis. *Bull. Amer. Meteor. Soc.*, 91, 1015–1057, doi: <http://dx.doi.org/10.1175/2010BAMS3001.1>.

Schlesinger, M. E., and N. Ramankutty (1994), An oscillation in the global climate system of period 65-70 years, *Nature*, 367(6465), 723-726.

Simmons, A., Uppala, C, Dee, D., and S. Kobayashi (2007): ERA-Interim: New ECMWF reanalysis products from 1989 onwards. ECMWF Newsletter No. 110, 25-35.

Stevens, B., M. Giorgetta, M. Esch, T. Mauritsen, T. Crueger, S. Rast, M. Salzmann, H. Schmidt, J. Bader, K. Block, R. Brokopf, I. Fast, S. Kinne, L. Kornblueh, U. Lohmann, R. Pincus, T. Reichler, and E. Roeckner (2013), Atmospheric component of the MPI-MEarth System Model: ECHAM6, *Journal of Advances in Modeling Earth Systems*, 5(2), 146–172.

Thompson, D. W. J., and J. M. Wallace (1998), The Arctic oscillation signature in the wintertime geopotential height and temperature fields, *Geophys Res Lett*, 25(9), 1297-1300, doi: 10.1029/98gl00950.

Vonder Haar, T. H., J. L. Bytheway, and J. M. Forsythe (2012), Weather and climate analyses using improved global water vapor observations, *Geophys Res Lett*, 39(15), doi: 10.1029/2012gl052094.

Walker, G. T. (1924), Correlations in seasonal variations of weather IX, *Mem. Ind. Meteor. Dept.*, 24, 275-332.

Zhang, Y., J. M. Wallace, and D. S. Battisti (1997), ENSO-like Interdecadal Variability: 1900–93, *J. Climate*, 10, 1004-1020.

8 Appendix A: Additional figures

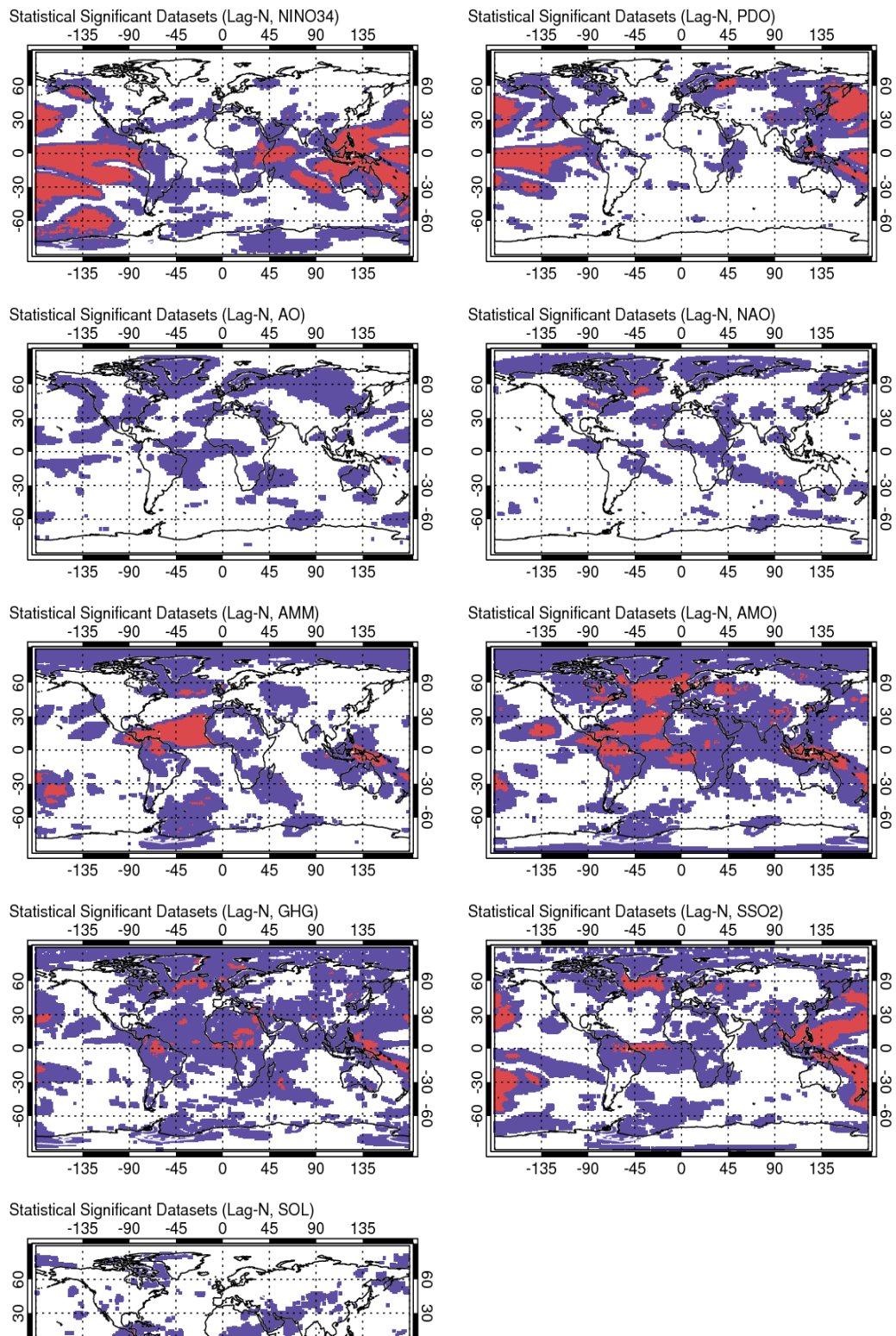


Figure 12: Same as Figure 7, but using Equation (2) to calculate N_{eff} .

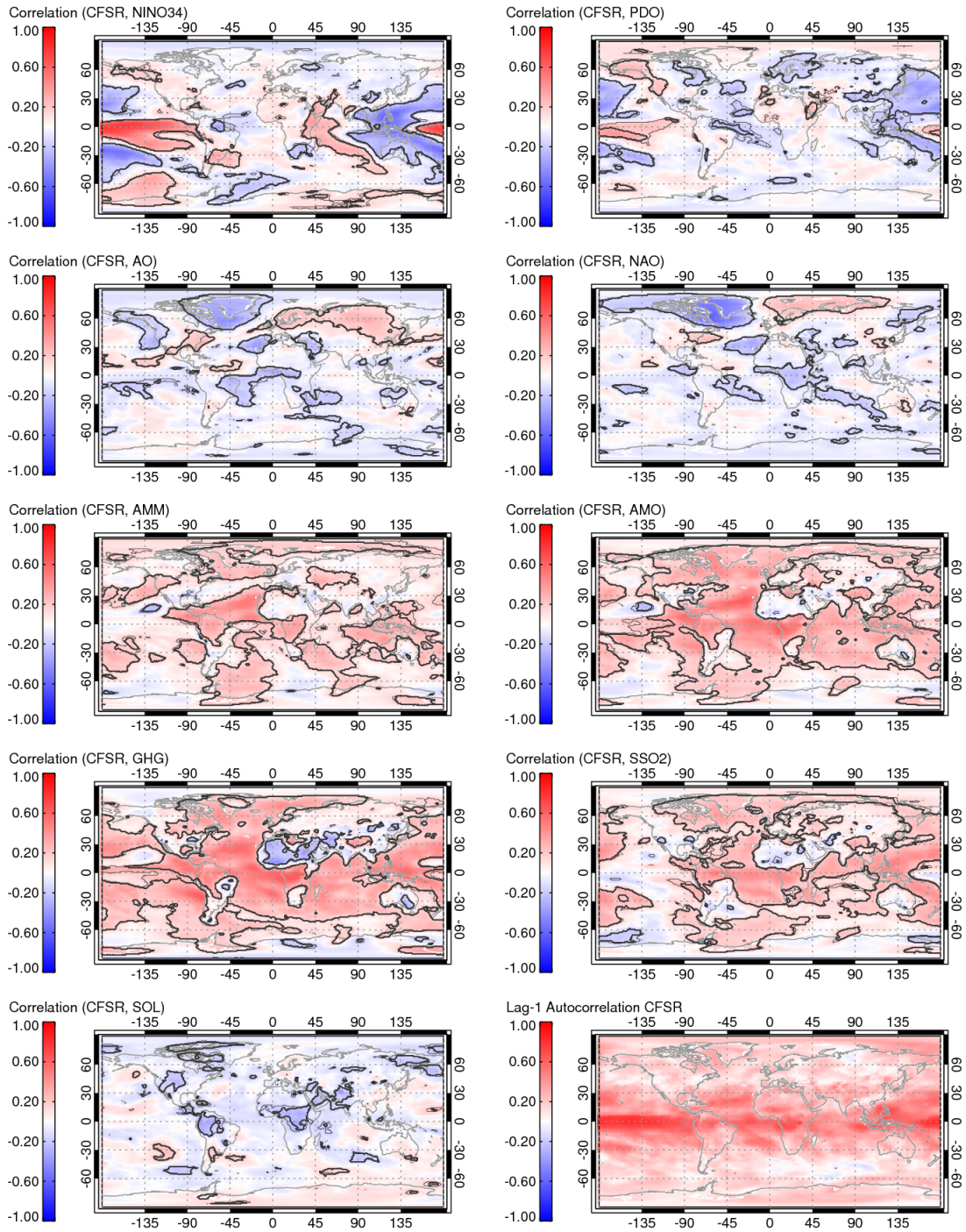


Figure 13: Same as Figure 6, but for CFSR.

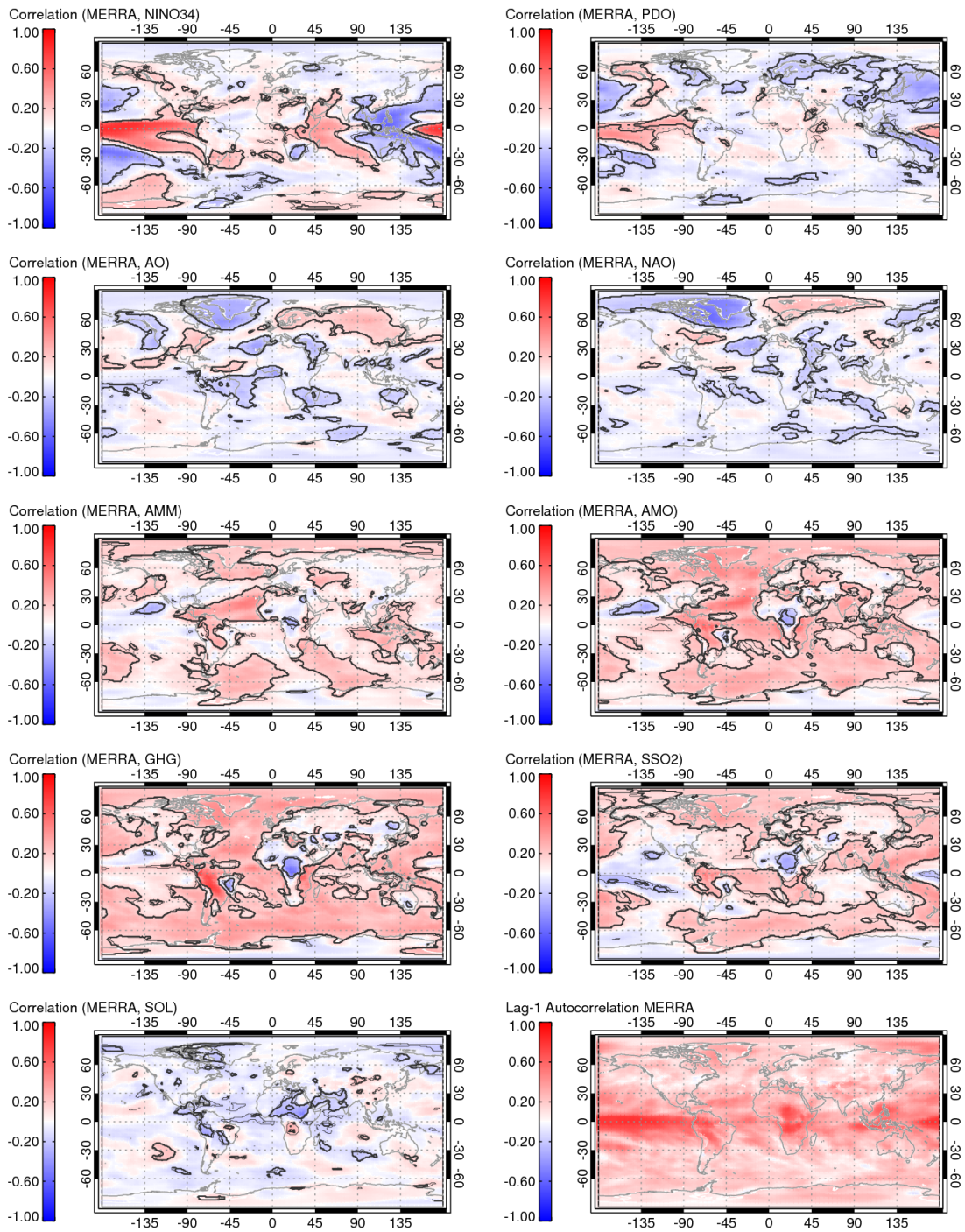


Figure 14: Same as Figure 6, but for MERRA.

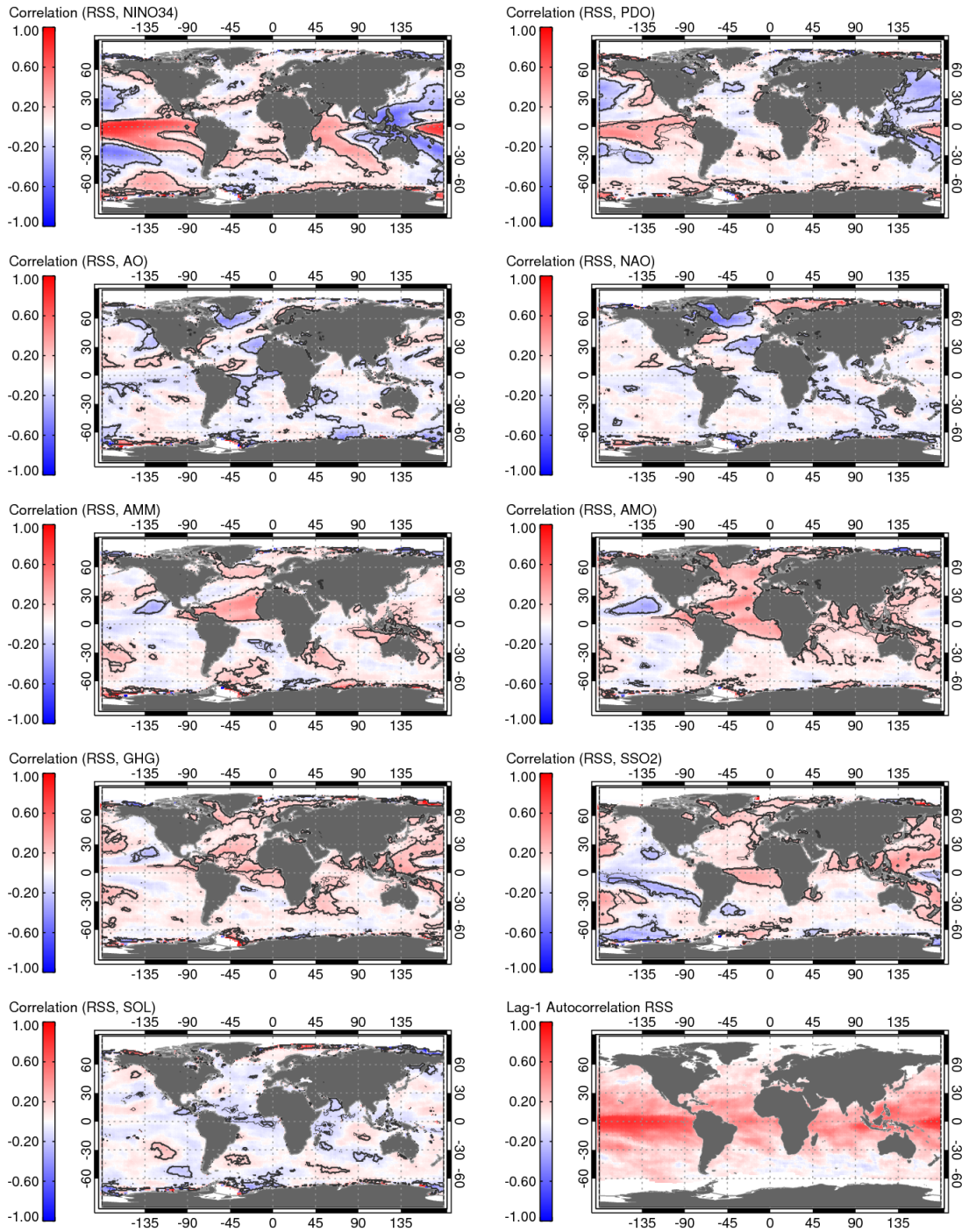


Figure 15: Same as Figure 6, but for RSS.

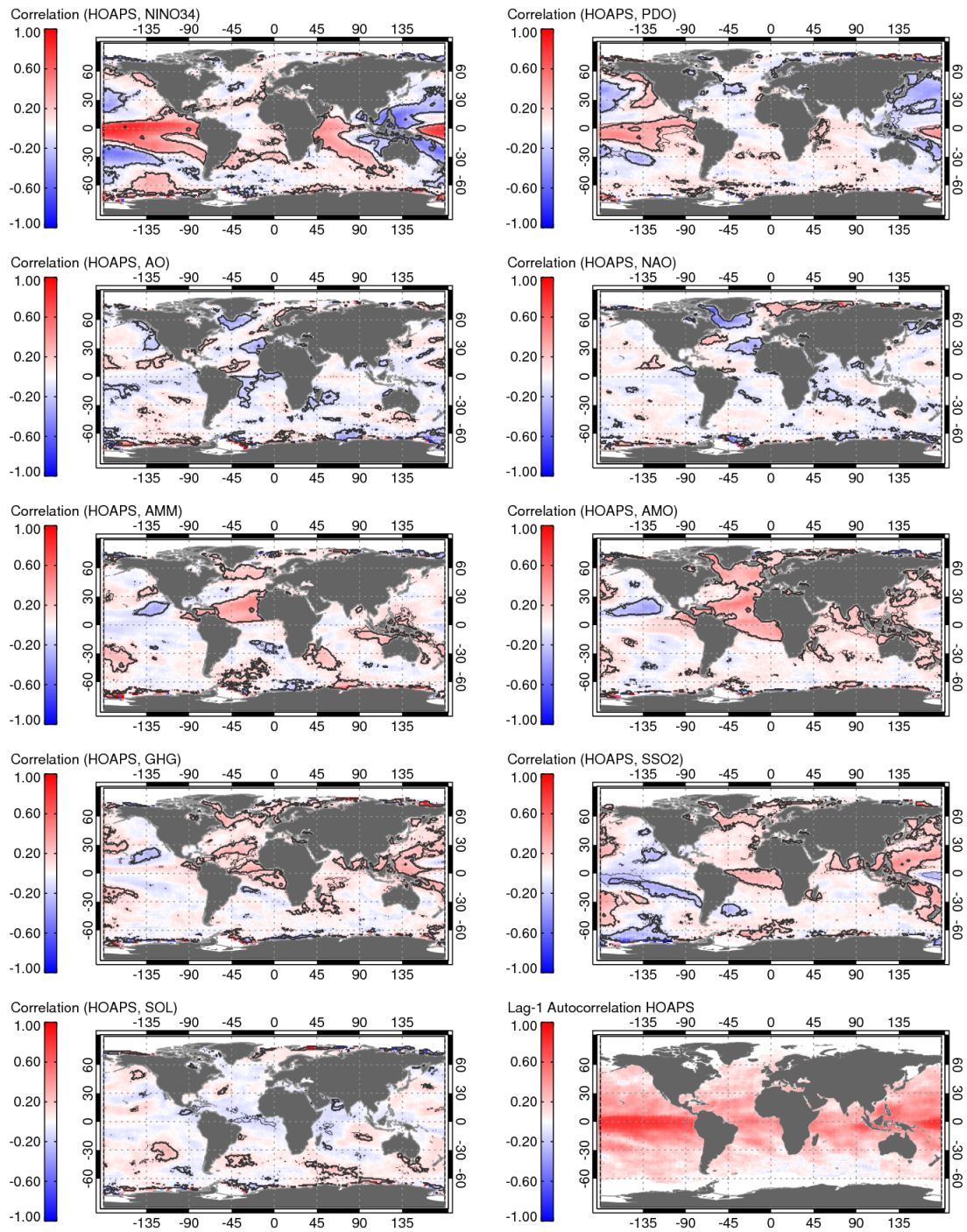


Figure 16: Same as Figure 6, but for HOAPS.

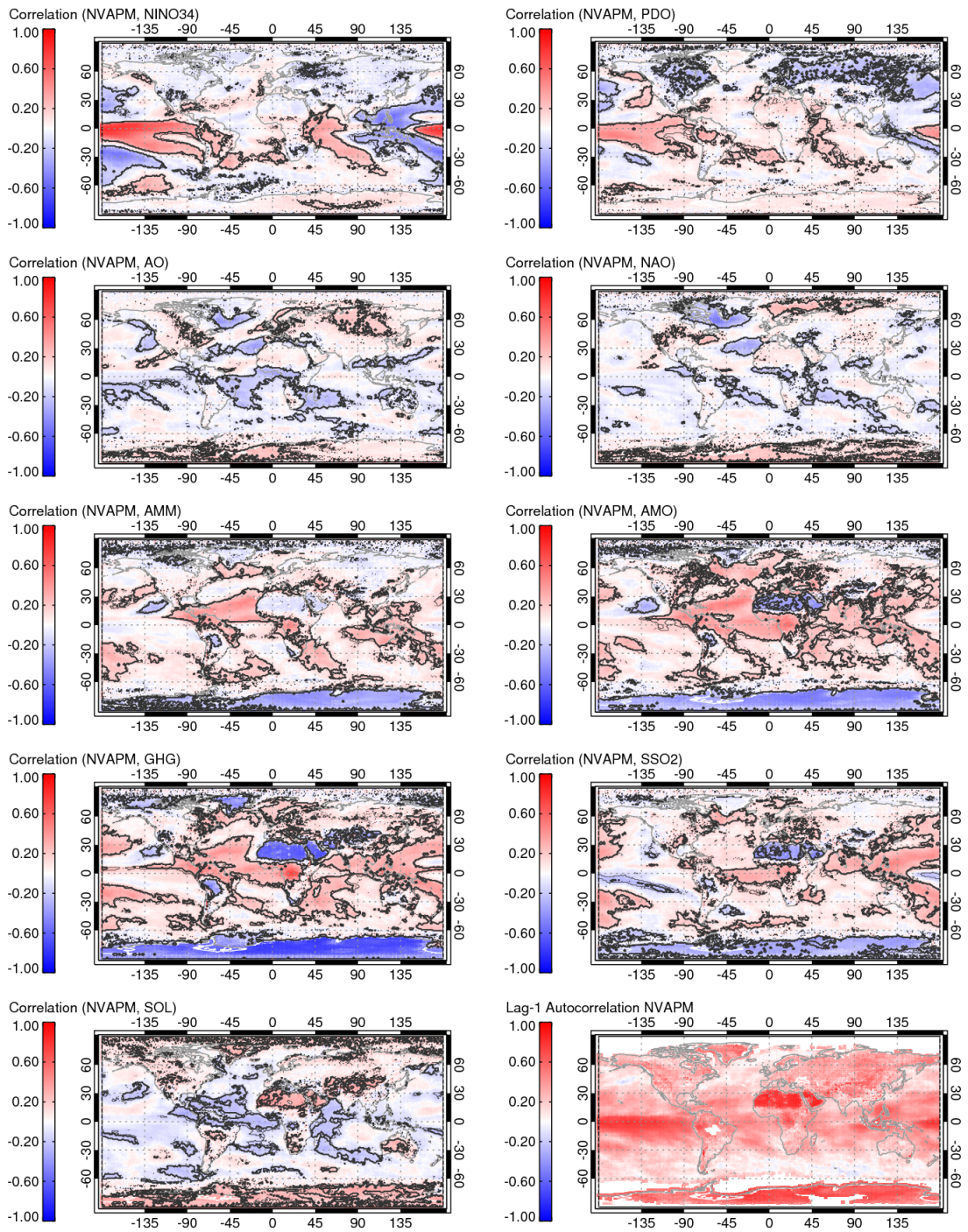


Figure 17: Same as Figure 6, but for NVAPM.

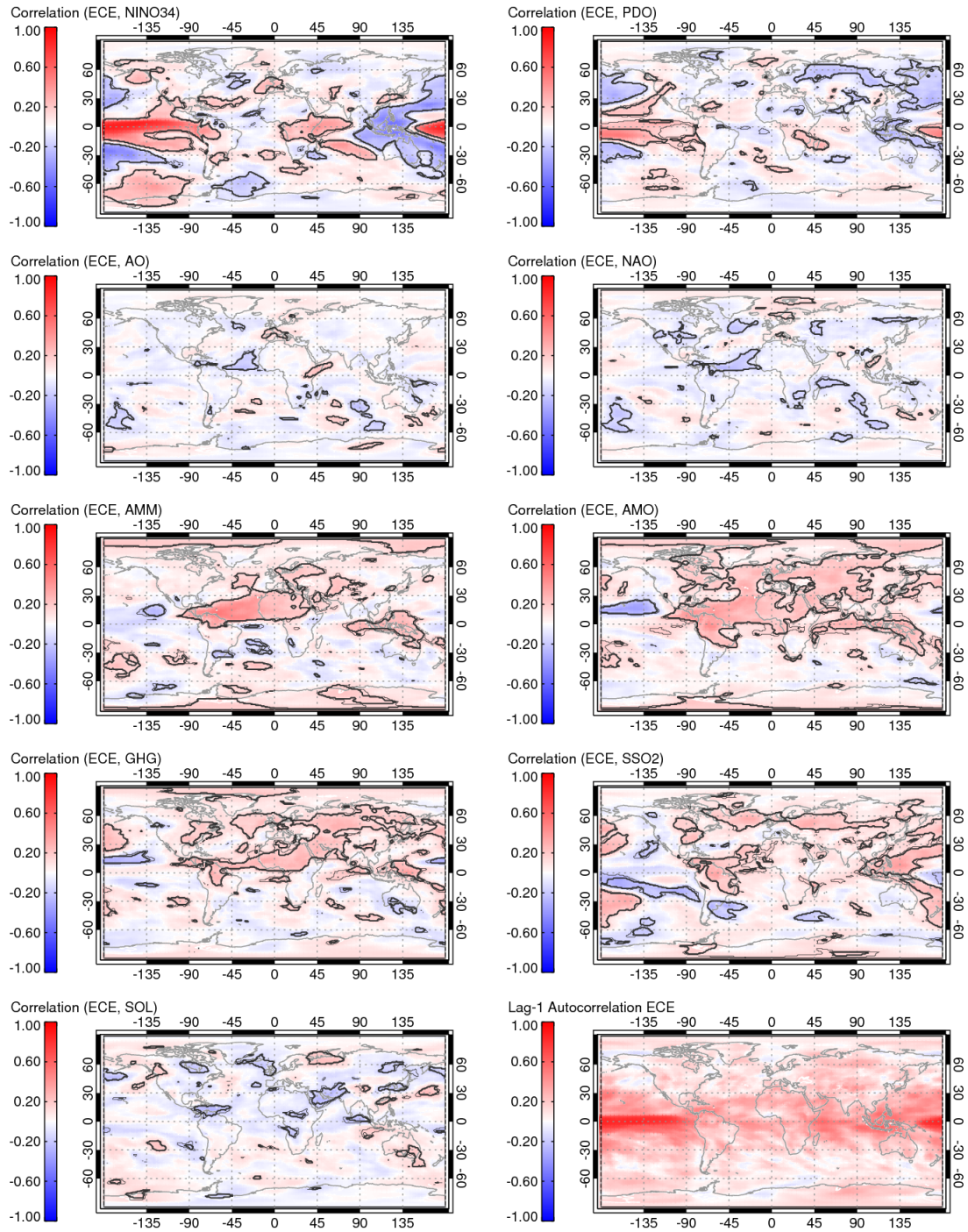


Figure 18: Same as Figure 6, but for EC Earth.

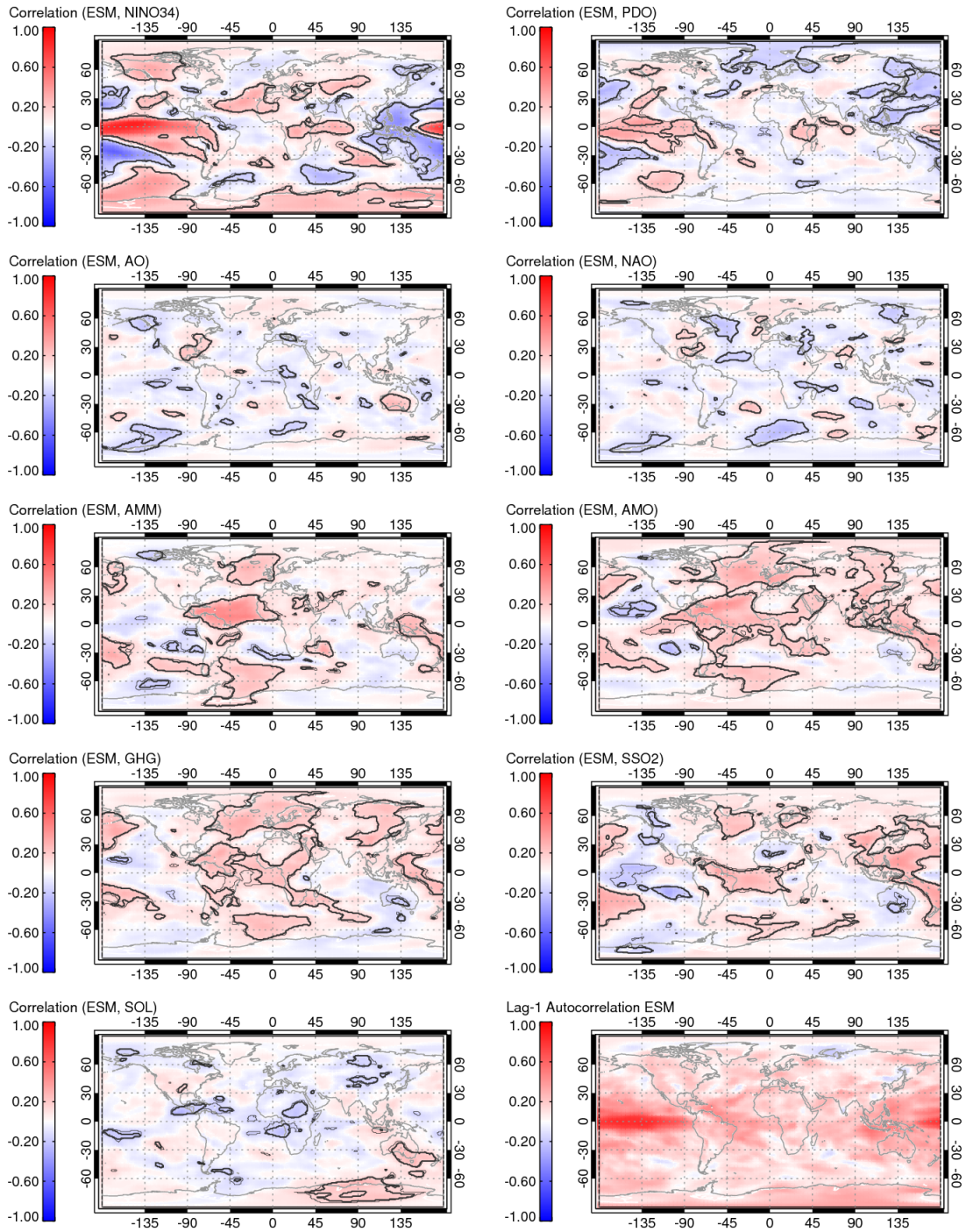


Figure 19: Same as Figure 6, but for ESM.

9 Appendix B: Description of output data

The root folder containing all VaKaS deliverables is hosted by DWD⁶. Inside the root folder, project deliverables are stored in a folder structure as follows:

```
[VAKAS root folder]/data
[VAKAS root folder]/results/maps_diff_month_since_1970
[VAKAS root folder]/results/time_series_alldata_regional
[VAKAS root folder]/results/time_series_climate_index
[VAKAS root folder]/results/correlation_maps
```

In the following subsections, we will shortly describe the contents of each folder.

9.1 [VAKAS root folder]/data

In order to enable an efficient processing of the investigated water vapour products, the original data products have been mapped onto a 1° by 1° longitude / latitude grid (360 x 180) at monthly temporal resolution and have then been stored in the NetCDF format. The resulting files (one for each of the considered products CSFR, ECE, ERA-Interim, ESM, HOAPS, MERRA, NVAPM, RSS) are available under [VAKAS root folder]/data. The file naming convention is:

```
VAKAS_<dataset_acronym>_<mmyyyy>_<mmyyyy>.nc,
```

where <dataset_acronym> indicates the considered water vapour product, the first (second)<mmyyyy> indicates the start (end) month and year of the period covered by the dataset.

Example: VAKAS_CFSR_011979_122008.nc contains CFSR re-gridded data for the period between January 1979 and December 2008.

The size of all files in [VAKAS root folder]/data amounts to 679 MB.

9.2 [VAKAS root folder]/results/maps_diff_month_since_1970

This folder holds images showing the global distribution of the Total Column Water Vapour (TCWV) in units of mm precipitable water. Each image shows the available products for one particular month as well the corresponding ensemble average value. The file naming convention is

```
maps_<month since January 1970>.jpg,
```

where <month since January 1970> is a three digit integer counting the months since the beginning of 1970, with January 1970 identified as month 000.

Example: maps_336.jpg, showing the global TCWV distribution for January 1998 (see Figure 20).

⁶ Please contact Marc Schroeder at Deutscher Wetterdienst (marc.schroeder@dwd.de) to obtain information on how to access the data.

Total Column Water Vapour [kg/m^2] January 1998

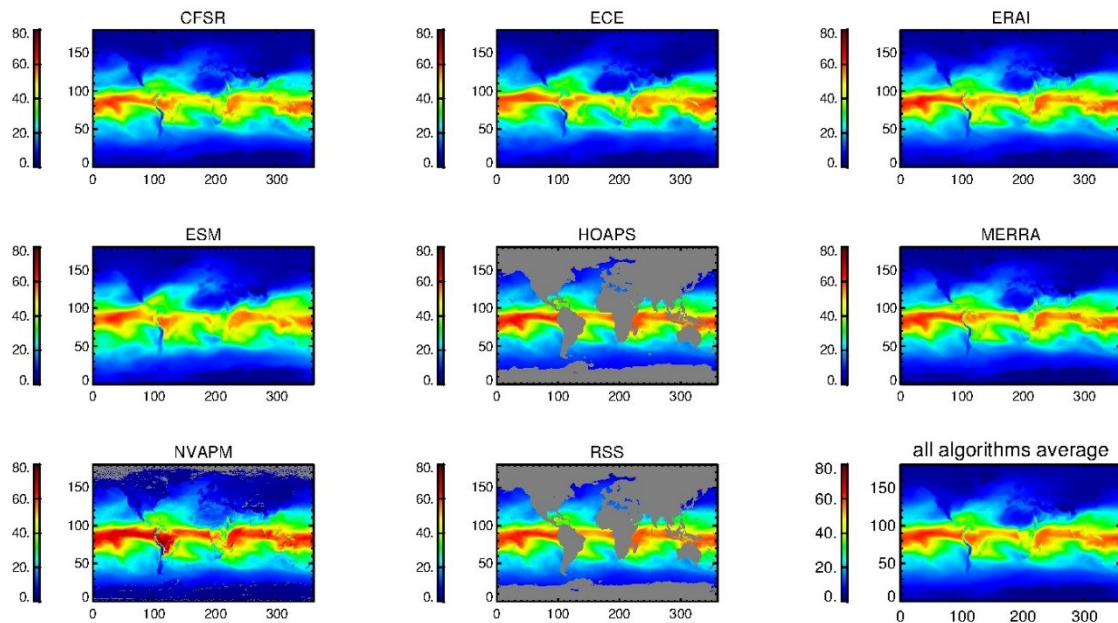


Figure 20: Image file “maps_336.jpg” showing the TCWV for all eight considered products as well as an all product average for January 1998.

The corresponding „diff“-files show the difference of each dataset to the ensemble average of the month. The filename convention is analogous to the „maps“-files:

diff_<month since January 1970>.jpg

Example: diff_336.jpg (see Figure 21).

Total Column Water Vapour – Difference to average [kg/m^2] January 1998

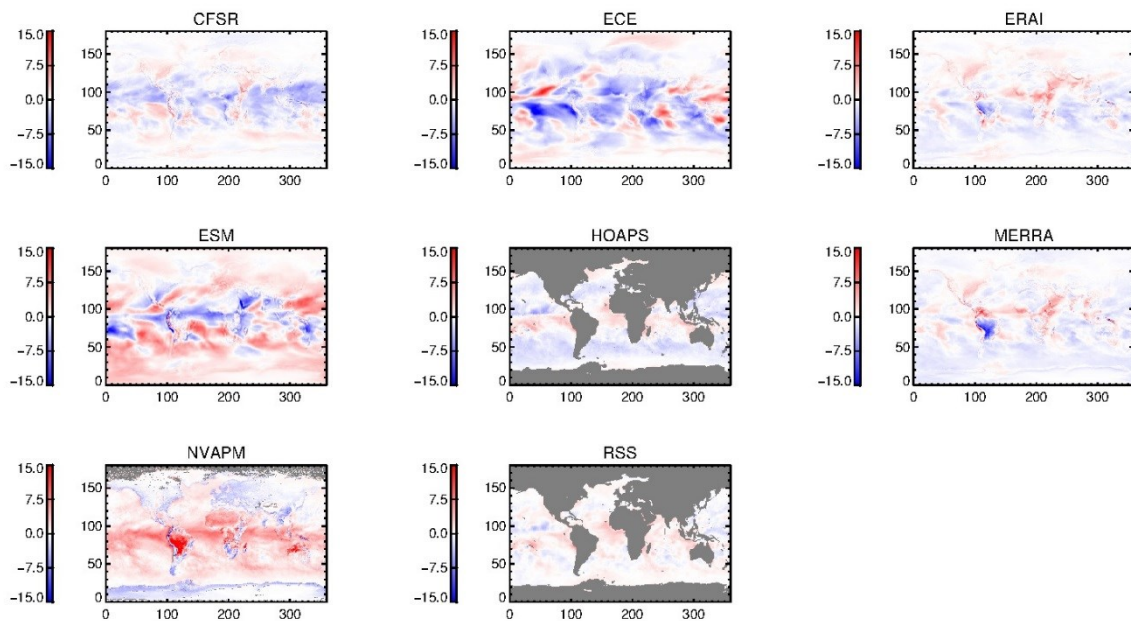


Figure 21: Image file diff_337.jpg showing differences from the average for the individual products.

The number of all files in [VAKAS root folder]/results/maps_diff_month_since_1970 amounts to 602 (301 map images plus 301 diff images), totalling 142 MB.

9.3 [VAKAS root folder]/results/time_series_alldata_regional

These image files in [VAKAS root folder]/results/time_series_alldata_regional combine the full time series for specific grid points. The file naming convention is:

ts_lon<lon_idx>_lat<lat_idx>.jpg,

where <lon_idx> is longitude value in degrees plus 180 and <lat_idx> is latitude in degrees plus 90. E.g., 1at_000 represents the latitude range between 90° S and 89°S and 1at_110 represents the latitude range from 20°N to 21°N. Analogously, 1on_250 represents the longitude range between 70° E and 71°E.

Example: ts_lon180_lat140.jpg (see Figure 22).

Images are provided for every 10-th degree latitude and longitude, amounting to $18 \times 36 = 648$ files. The total size of [VAKAS root folder]/results/time_series_alldata_regional amounts to 413 MB.

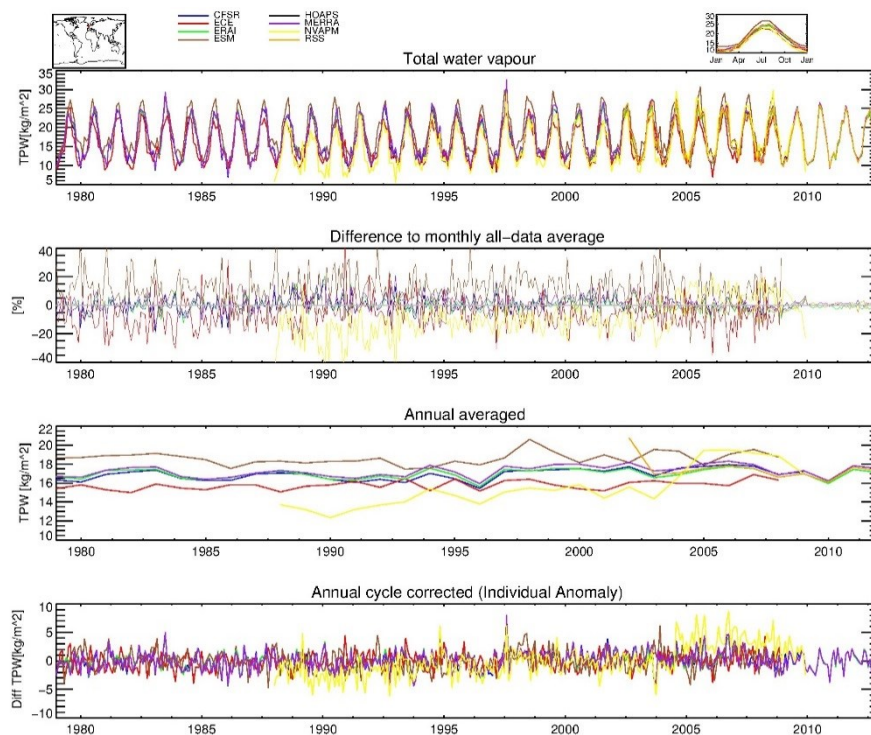


Figure 22: Image file “ts_lon180_lat140.jpg” showing the time series for all datasets at the grid cell at 0°E and 50°N.

Shown in each image file are from top to bottom:

- TCWV value [kg/m²],
- Relative difference to the ensemble monthly mean [%],
- Annually averaged TCWV [kg/m²],

- Time series corrected for seasonal effects [kg/m²].

The inset on the top left indicates the position of the grid box considered. The average annual cycle for all investigated time series is shown in the inset at the top right.

9.4 [VAKAS root folder]/results/time_series_climate_index

The folder [VAKAS root folder]/results/time_series_climate_index contains time series of the six core climate indices considered in this study. The file naming convention is:

```
<ci_acronym>.jpg,
```

where <ci_acronym> represents an acronym used to identify a specific climate index.

Example: nino34.jpg (see Figure 23).

The number of all files in [VAKAS root folder]/results/time_series_climate_index amounts to 6, totalling 0.5 MB.

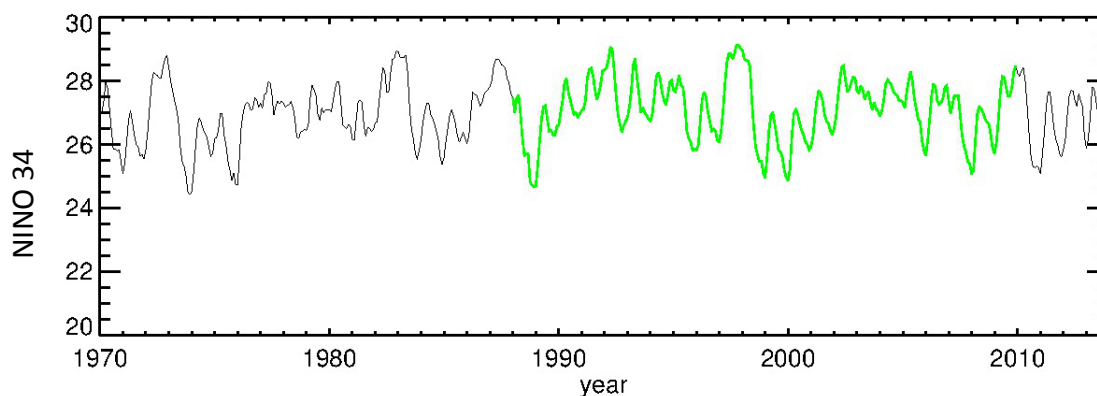


Figure 23: Image file "nino34.jpg" showing the long-term time series of the NINO34 climate index. The green colour indicates the core VAKAS period 1988-2008.

9.5 [VAKAS root folder]/results/correlation_maps

The folder [VAKAS root folder]/results/correlation_maps holds maps showing the correlation between observational time series and climate indices. The file naming convention is:

```
corr_map_<data>_<climate>_<period>.jpg,
```

where <data> is the dataset acronym, <climate> indicates the climate index and <period> designates the considered seasonal range.

For each combination of dataset and core climate index, three periods have been considered: jja – June/July/August (northern summer), djf – December/January/February (northern winter), as well as the entire year if <period> is empty).

Example: corr_map_HOAPS_ao_jja.jpg (see Figure 24), representing the correlation map of HOAPS with the AO climate index in the northern summer months.

The number of all files in [VAKAS root folder]/results/correlation_maps amounts to 144, totalling 54 MB.

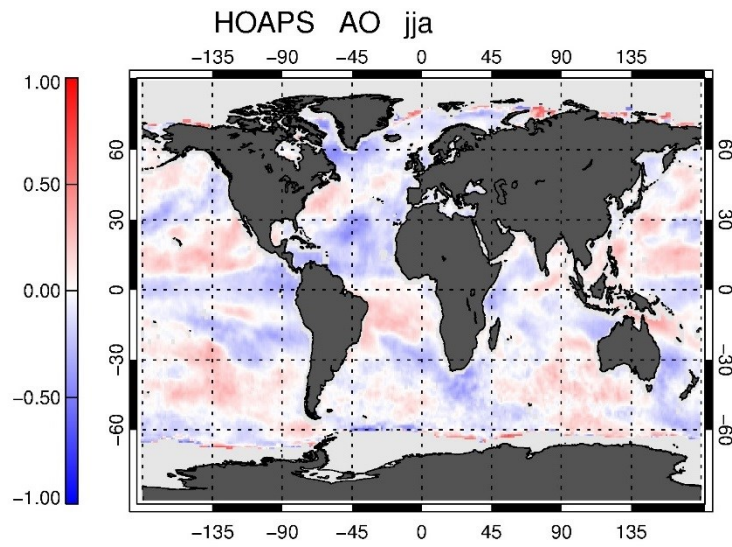


Figure 24: Image file “corr_map_HOAPS_AO_jja.jpg” showing the correlation between HOAPS and the AO climate index for the northern summer months.